

QUANTIFICATION OF ULTRASOUND CONTRAST AGENTS USING  
HIGH-FREQUENCY ULTRASOUND

BY

DARRYL C. MA

B.S., University of Illinois at Urbana-Champaign, 2007

THESIS

Submitted in partial fulfillment of the requirements  
for the degree of Master of Science in Electrical and Computer Engineering  
in the Graduate College of the  
University of Illinois at Urbana-Champaign, 2009

Urbana, Illinois

Adviser:

Assistant Professor Michael L. Oelze

## ABSTRACT

Ultrasound contrast agents (UCAs) are small microbubbles filled with gas. Because of their scattering properties, UCAs enhance the diagnostic capabilities of ultrasonic imaging. UCAs are associated with therapeutic or enhancing therapeutic applications of ultrasound and with possible adverse bioeffects. Quantification of the in vivo concentration of microbubbles is therefore essential to establishing a dose/effect response for therapeutics and for quantifying other bioeffects. The concentration of UCAs is hypothesized to be proportional to the magnitude of the ultrasonic backscattered power spectrum. To demonstrate the ability to quantify UCAs from ultrasonic backscatter, several experiments were conducted. All experiments were conducted with FDA approved Definity® contrast agents and were performed in vitro, i.e., within a beaker or within a perfusion phantom, or in vivo, i.e., within the auricular artery of a rabbit. Estimates of the UCA concentration were obtained by comparing estimates of the backscattered power spectrum corresponding to the scattering from UCAs. A Monte Carlo technique was used to estimate the UCA concentration in vitro by minimizing the mean square error between the estimated power spectrum and the theoretical power spectrum. Samples of the Definity mixture were also extracted and analyzed under a fluorescence microscope and hemacytometer to obtain the size distribution and concentration of microbubbles optically for comparison with the ultrasound estimates. In both the in vitro and in vivo experiments, the linear relationship between the UCA concentration and magnitude of the ultrasonic backscattered power spectrum was demonstrated. Additionally, with the Monte Carlo technique, the UCA concentration and mean microbubble radius was estimated to within 12.3% and 8.48% of the optically measured values, respectively.

# TABLE OF CONTENTS

CHAPTER 1: INTRODUCTION .....	1
1.1 Motivation.....	1
1.2 Background Literature Review .....	1
1.3 Organization of Thesis.....	3
CHAPTER 2: THEORY AND SIMULATIONS .....	4
2.1 What is an Ultrasound Contrast Agent?.....	4
2.2 Description of the Backscattered Signal and Backscatter Cross Section .....	5
2.3 Theoretical Backscatter Cross Section.....	6
2.4 Building the Theoretical Model.....	9
2.4.1 The inverse polytropic coefficient and surface tension coefficient .....	9
2.4.2 Resonant frequency for various bubble diameters.....	10
2.4.3 Damping coefficient vs. diameter of microbubbles.....	10
2.4.4 Scattering cross section vs. frequency .....	11
2.5 Theoretical Backscatter Cross Section vs. Frequency .....	11
2.6 Measured Backscatter Cross Section .....	12
2.7 Attenuation Coefficient.....	13
2.8 Figures.....	14
2.9 Tables.....	20
CHAPTER 3: METHODS AND MATERIALS .....	22
3.1 Properties of Transducers .....	22
3.2 In Vitro Experiments.....	23
3.2.1 Beaker experiments.....	23
3.2.2 Perfusion phantom experiments.....	24
3.3 In Vivo Experiments .....	26
3.4 Optical Estimation of Microbubble Concentration.....	27
3.5 Estimating UCA Size Distribution.....	27
3.5.1 Image analysis in the spatial domain .....	28
3.5.2 Image analysis in the frequency domain.....	28
3.5.3 Test of image processing accuracy with latex spheres .....	29
3.6 Monte Carlo Simulation.....	29
3.7 Figures.....	31
3.8 Tables.....	40
CHAPTER 4: RESULTS.....	42
4.1 In Vitro Experiments.....	42
4.1.1 Beaker experiments.....	42
4.1.2 Perfusion phantom experiments.....	44
4.2 Concentration of UCA Population.....	45
4.3 Size Distribution of UCA Population .....	46
4.4 In Vivo Experiments.....	47
4.4.1 In vitro backscatter power measurements in blood medium .....	47

4.4.2 In vivo experiments within central auricular artery .....	48
4.5 Theory vs. Measured Backscatter Cross Section .....	49
4.6 Figures .....	51
4.7 Tables .....	67
CHAPTER 5: CONCLUSIONS AND FUTURE WORK .....	72
5.1 In Vitro Experiments .....	72
5.1.1 Beaker experiments .....	72
5.1.2 Perfusion phantom experiments .....	73
5.2 In Vivo Experiments .....	73
5.3 Concentration of UCA Population .....	74
5.4 Theory vs. Measured Backscatter Cross Section .....	74
5.5 Future Work .....	75
REFERENCES .....	76

# CHAPTER 1: INTRODUCTION

Ultrasound contrast agents (UCAs) have played a pivotal role in clinical examinations and therapeutic techniques since the 1960s. Some of the possible applications of UCAs include contrast enhancement between blood vessels and background tissue, perfusion imaging, facilitating thrombolysis (i.e., breakdown of blood clots), and gene and drug delivery [1]. In addition, possible adverse bioeffects have also been attributed to the use of UCAs. Because of their breadth of application, much research has been conducted to understand, characterize, and model the ultrasound backscatter properties of UCAs. However, a technique to quantify the concentration of UCAs in vivo in order to establish a dose-effect-response is needed to continue advancing research in this area.

## 1.1 Motivation

Recent studies have resulted in theoretical models that correlate well to measured backscatter data, opening up possibilities for monitoring of UCA dose in vivo ([2], [3], [4], [5]). The purpose of this study is to develop a technique to quantify UCA dose in vivo versus time. Because the possibility of bioeffects has been hypothesized to increase with the presence of UCAs in the blood acting as cavitation sites, the ability to quantify UCA concentration in the blood would allow dose-effect-response curves to be established. We hypothesize that the concentration of UCAs at any instant in time can be estimated through parameterization of the normalized backscatter power spectrum. In this thesis, our goal is to develop a technique to quantify UCAs in vitro and in vivo based on the normalized backscattered power spectrum, enabling the tracking of microbubble concentrations noninvasively within the body.

## 1.2 Background Literature Review

Since the 1940s, it has been of interest to researchers to characterize the behavior of air bubbles in the presence of an acoustic field. Initially, the motivation to understand bubble behavior was to compensate for acoustic signal degradation resulting from clouds of air bubbles in the ocean. However, in the 1960s, what had been deemed a limitation

was instead manipulated for benefiting diagnostic ultrasound imaging – the intense backscatter properties of air bubbles that limited the range of sonar were used instead to enhance contrast within the body. Since then, numerous studies have been conducted into understanding the behavior of bubbles in a sound field.

In 1992, de Jong et al. [2] successfully demonstrated the linear relationship between concentrations of Alunex microbubbles and scattered power. They also observed substantial correlation between theoretical transmitted and scattered power models from clouds of Alunex microbubbles and obtained data up to 12.5 MHz. However, they reported that the models for the “acoustical behavior of Alunex microspheres were far better at describing behavior of larger microspheres than smaller ones” [2]. Because smaller microspheres have a higher resonant frequency, their findings suggest that the proposed model may be inadequate for predicting microbubble behavior at higher frequencies. Nevertheless, success in predicting the frequency dependent behavior for Alunex microbubbles and later Myomap™ and Quantison™ microbubbles demonstrated the robustness of the model. Based on the success of the models developed by de Jong et al. [2], we intend to solve the inverse problem using ultrasound backscattered data and estimate the UCA concentration ([3] and [4]).

Most of de Jong’s work focused on albumin shelled microbubbles, which Dayton et al. have demonstrated to behave very differently, both acoustically and optically, from lipid shelled UCAs such as Definity® [6]. In 2007, Goertz et al. were able to obtain shell parameter values and shell friction estimates for Definity® microbubbles by fitting attenuation data to theoretical models [7]. Unfortunately, to date no other studies have been conducted to corroborate the Definity® results provided by Goertz et al.

In addition, all studies mentioned above have been conducted in vitro. In a step intended to move closer to an in vivo system, Bridal et al. attempted to quantify SonoVue™ or EchoGen® microbubbles in an in vitro perfusion phantom. The perfusion phantom was used because it more closely emulates the cardiovascular system. However, few have attempted to tackle the problem of quantifying UCAs in vivo, which is a far more complicated problem due to the interference of backscatter from blood [8]. This study aspires to build on the work accomplished by past researchers and extend the realm of UCA quantification into the in vivo setting.

### **1.3 Organization of Thesis**

This thesis is organized as follows: Chapter 2 presents the theory and simulation data obtained in the process of constructing the theoretical backscatter cross section model. Chapter 3 describes the methods and materials used in various experiments to quantify Definity® microbubbles. Chapter 4 discusses the results of these experiments and Chapter 5 presents conclusions and offers suggestions for future work.

## CHAPTER 2: THEORY AND SIMULATIONS

The main purpose of this chapter is to familiarize the reader with some background theory on scattering from UCAs and demonstrate the validity of the computer code written to predict the theoretical backscatter cross section of UCAs. Various parameters were derived with the code and compared to results obtained by previous researchers. In addition, the formulation of the inverse problem will also be detailed in this chapter. The inverse problem formulation is the method by which estimates of the UCA concentration are extracted from ultrasound backscatter measurements.

### 2.1 What is an Ultrasound Contrast Agent?

A UCA is a microbubble that consists of a gas core encapsulated within a shell. Microbubbles without a shell are known as *free bubbles*. The gas cores are usually composed of air or heavy gases such as perfluorocarbons or nitrogen. Heavy gases reduce the likelihood of the gas diffusing into the surrounding liquid medium, thereby increasing the lifetime of the microbubble. The lifetime of microbubbles in solution is further prolonged by the inclusion of a 10-200 nm thick shell, composed of either albumin, galactose, lipids, or polymers. The engineering tradeoff for extending the lifetime of these microbubbles in solution, however, is a reduction in the power scattered by these microbubbles at the fundamental frequency of ultrasound used to insonify the UCAs and subsequent harmonics. Free bubbles have been observed to backscatter ultrasound more efficiently due to the absence of a shell which damps the acoustic signal [1]. Another side-effect of the microbubble shell is an increase in the resonant frequency of the bubble [1].

In 1999, Dayton et al. [6] observed optically and acoustically that differences in the shell material and gas core can drastically affect the UCA's lifetime, acoustic response, and mechanism leading to microbubble destruction. Depending on the stiffness of the microbubble shell, volatility of the gas core, and size of the microbubble, Dayton et al. [6] outlined four different mechanisms for the destruction of contrast agents: (1) microbubbles can gradually decrease in size as gas diffuses out, (2) the ultrasound beam

can induce a shell defect, which allows gas to escape, (3) the UCAs can fragment into smaller bubbles under the pressure of an acoustic field, or (4) the UCAs can rapidly self-destruct, expelling shell material away from the core.

In our experiments, we used Definity® microbubbles, which are microspheres composed of nonflammable gaseous octafluoropropane encapsulated within a perflutren lipid shell. The mean diameter of these microspheres as reported by the manufacturer ranges from 1.1 to 3.3  $\mu\text{m}$  with 98% of the particle population being less than 10  $\mu\text{m}$  in diameter and a maximum diameter of 20  $\mu\text{m}$ . After Vialmix® activation, 1 mL of Definity contains approximately  $1.2 \times 10^{10}$  perflutren lipid microspheres.

When UCAs are acoustically excited, because of the acoustic impedance mismatch between the encapsulated gas and surrounding fluid, the bubbles compress, oscillate and reflect a characteristic echo. When these microbubbles are injected into a patient's bloodstream, the unique echoes produced by the UCAs amplify contrast between the bloodstream and background tissue, enabling clinicians to better diagnose occlusions and other irregularities in a blood vessel.

In this study, we compared the backscattered power for three different concentrations of Definity for both in vitro and in vivo experiments. Clinically, the standard is to administer 0.5 mL of Definity to a human being (~6.2 liters of blood) for a single examination. For our in vitro experiments, we conducted experiments at 0.1, 1 and 2 times the standard dosage in 250 mL of degassed water. For the in vitro experiments, through analysis of the backscattered power from a cloud of microbubbles, we hypothesize that we can quantify the concentration of microbubbles.

## **2.2 Description of the Backscattered Signal and Backscatter Cross Section**

The backscattered signal/echo is the acoustic signal that is reflected back to the source of the acoustic field. For a given acoustic scatterer, the frequency dependence of the characteristic backscattered echo is dependent on the size, shape and elastic properties of the scattering medium while the amplitude of the backscattered echo depends on the size, density and scattering strength (i.e., fractional variation in acoustic impedance) [9].

In this study, the backscatter will be quantified in terms of the backscatter cross section. The backscatter cross section is related to the backscatter coefficient by a

normalization factor, i.e., dividing by the resolution cell volume (see Equation (2.3)). All frequency and scatterer size dependent characteristics of the backscatter coefficient hold for the backscatter cross section and vice versa. For the purposes of this study, the backscatter coefficient and backscatter cross section are used interchangeably. The backscatter cross section is defined as the fraction of energy a scatterer extracts from a sound beam of  $1 \text{ m}^2$  cross section and redirects back to the source and is usually two to three orders of magnitude larger than its geometric cross section [10].

Changes in the size of the scatterer have a greater effect on the magnitude of the backscatter coefficient than changes in the concentration of scatterers. The magnitude of the backscatter coefficient includes everything in Equation (2.1) [11] except the form factor,  $F(f, D)$ ,

$$\sigma_b(f) = Cf^4 D^6 \bar{n} \gamma_0^2 F(f, D) \quad (2.1)$$

where  $C = (\pi^4/36c^4)$ ,  $c$  is the speed of sound in the medium,  $f$  is the frequency,  $D$  is the diameter of the scatterer,  $\bar{n}$  represents the number of scatterers per unit volume,  $\gamma_0^2$  is the mean-squared variation in acoustic impedance between scatterer and surrounding medium, and  $F(f, D)$  is called the form factor and is a function of frequency and scatterer diameter. Because the volume of a sphere is  $4/3\pi r^3$  and because the backscatter coefficient is proportional to  $D^6$ , it follows that the backscatter coefficient is proportional to the square of the scatterer's volume. On the other hand, the concentration of scatterers,  $\bar{n}$ , varies only linearly with the backscatter coefficient, indicating that the changes in average size of the scatterers typically result in greater changes in magnitude of the backscattered power than changes in concentration of scatterers.

### 2.3 Theoretical Backscatter Cross Section

Before proceeding any further, it should be noted that all equations below will be presented without any formal explanation. It is beyond the scope of this paper to describe the derivation process in detail. For a comprehensive description of these equations and their derivations, refer to Medwin [12], de Jong et al. [13], Doinikov et al. [14], Leighton [15], Cornet et al. [16], and Devin [17].

The scatter cross section and scatter coefficient for a single spherical scatterer are described by Medwin [12] and de Jong et al. [13] as:

$$\sigma_s = \frac{4\pi r^2}{\left(\frac{f_r^2}{f^2} - 1\right)^2 + \delta^2} \quad (2.2)$$

$$\sigma_{sc} = \frac{\sigma_s}{V} \quad (2.3)$$

where  $r$  is the radius of scatterer,  $f_r$  is the resonance frequency of scatterer,  $f$  is the frequency of applied ultrasound field,  $\delta$  represents the total damping due to thermal conductivity, viscosity, and reradiation, and  $V$  is the volume of the resolution cell.

The above equations represent the total power scattered over all angles. To obtain the backscatter cross section, the following conversion is applied:

$$\sigma_{bs} = \frac{A^2}{4z^2} \sigma_s \quad (2.4)$$

where  $A$  is the radius of the transducer, and  $z$  is the distance from the scattering volume to transducer.

The resonant frequency of a microbubble with an elastic shell is given by

$$f_r = \frac{\sqrt{\frac{S_a}{m} b \beta + \frac{8\pi S_p}{m}}}{2\pi} \quad (2.5)$$

where  $S_a$  is the adiabatic stiffness of the gas,  $m$  is the effective mass of the system,  $b$  is the inverse of the polytropic coefficient,  $\beta$  is the surface tension coefficient, and  $S_p$  is called the shell parameter [2]. The effective mass of the system is defined as

$$m = 4\pi r^3 \rho \quad (2.6)$$

where  $r$  is the radius of the scatterer and  $\rho$  is the water density. The adiabatic stiffness of the gas is given by

$$S_a = 12\pi r \gamma P_0 \quad (2.7)$$

where  $\gamma$  is the ratio of specific heats for octofluoropropane,  $P_0$  is the ambient static pressure, and

$$b = \left[ 1 + (d/b)^2 \right]^{-1} \left[ 1 + \frac{3(\gamma-1)}{X} \left( \frac{\sinh X - \sin X}{\cosh X - \cos X} \right) \right]^{-1} \quad (2.8)$$

$$d/b = 3(\gamma-1) \left[ \frac{X(\sinh X - \sin X) - 2(\cosh X - \cos X)}{X^2(\cosh X - \cos X) + 3(\gamma-1)X(\sinh X - \sin X)} \right] \quad (2.9)$$

$$X = r(2\omega\rho_g C_{pg} / K_g)^{1/2} \quad (2.10)$$

$$\rho_g = \rho_{gA} [1 + 2\tau / (P_0 r)] \quad (2.11)$$

where  $\omega$  is the angular frequency,  $\rho_g$  is the density of the encapsulated gas,  $\rho_{gA}$  is the density of free gas at sea level,  $C_{pg}$  is the specific heat at constant pressure of gas,  $K_g$  is the thermal conductivity of gas, and  $\tau$  is the surface tension. The surface tension coefficient is given by

$$\beta = 1 + [2\tau / (P_0 r)] [1 - 1 / (3\gamma b)]. \quad (2.12)$$

The damping coefficient is given by

$$\delta = \delta_{rad} + \delta_{vis} + \delta_{th} + \delta_{fr} \quad (2.13)$$

where the damping due to radiation is

$$\delta_{rad} = kr \quad (2.14)$$

the damping due to viscosity is

$$\delta_{vis} = 4 \frac{\eta}{\rho\omega r^2} \quad (2.15)$$

the damping due to thermal conductivity is

$$\delta_{th} = (d/b) \left( \frac{f_r^2}{f^2} \right) \quad (2.16)$$

and the damping due to shell friction is

$$\delta_{fr} = \frac{S_f}{m\omega} \quad (2.17)$$

where  $k$  is the wave number,  $\eta$  is the shear viscosity of liquid, and  $S_f$  is the shell friction [2]. Table 2.1 lists the values and offers a brief description of some of the parameters mentioned above for Definity microbubbles ([12] and [16]).

The damping coefficients mentioned above take into account the loss of energy due to sound radiation, viscous forces at the gas-liquid interface, thermal conduction between the gas in the bubble and the surrounding liquid, and shell friction [17].

Damping due to reradiation is incorporated to compensate for the loss of energy in the bubble system because of the reradiation of spherical sound waves. These reradiated sound waves are frequently referred to as the scattered signal. Viscous damping occurs because there are viscous forces that exert an excess pressure at the gas-liquid interface of the bubble. Excess pressure caused by viscous forces is the result of a transfer of momentum from one region of the liquid to another moving at different velocity. Because of this excess pressure, more energy is required to compress the bubble than is regained in the subsequent expansion [17]. Thermal damping arises when the driving pressure at the bubble surface compresses the bubble, applying work on the gas space. This work increases the internal energy of the gas, resulting in a transfer of heat energy throughout the gas [17]. A fraction of this added heat energy is lost into the surrounding liquid via conduction. The thermal damping coefficient accounts for this heat energy loss. Damping due to shell friction considers the energy loss as a result of internal friction, or viscosity, within the shell material. The degree of energy loss is determined by the elasticity of the shell material,  $S_f$  [2].

## 2.4 Building the Theoretical Model

To verify the accuracy of the theoretical model, various parameters were plotted and tabulated and compared against results obtained by de Jong et al. [13] and Medwin [12]. This section documents the succession of parameters required to obtain the final theoretical backscatter cross section. Since each successive parameter builds upon the previous parameters, accuracy at each parameter should ensure overall correctness.

### 2.4.1 The inverse polytropic coefficient and surface tension coefficient

The inverse polytropic coefficient,  $b$ , given by Equation (2.8) and surface tension coefficient,  $\beta$ , given by Equation (2.12) directly determine the value of the damping coefficient due to thermal conductivity,  $\delta_{th}$  (see Equation (2.16)), and more importantly, the resonant frequency (see Equation (2.5)) at which the scatterer oscillates. Congruence between Figure 2.1a and Figure 2.1b illustrates that the inverse polytropic coefficient,  $b$ , and surface tension coefficient,  $\beta$ , were accurately reproduced with our code.

## 2.4.2 Resonant frequency for various bubble diameters

Table 2.2a and Table 2.2b illustrate the relationship between the resonant frequency of a bubble and the bubble diameter and shell parameter,  $S_p$ . Simulations predict that resonant frequency (see Equation (2.5)) increases as the bubble diameter decreases and shell parameter increases. According to Frinkling et al. [3], the shell parameter describes the compressibility of the shell. Analogous to the spring constant,  $k$ , in Hooke's law,  $F = -kx$ , which determines the natural frequency at which a spring oscillates,  $\omega = \sqrt{k/m}$  ( $m$  is the mass attached to the spring), the shell parameter determines the strength of the restoring force exerted by the shell. The stronger the restoring force, the higher the resonant oscillation. Minor differences in the resonant frequency values between Table 2.2a and Table 2.2b are likely the result of different values used for certain parameters (e.g.,  $\rho_{gA}$ ,  $C_{pg}$ ,  $\gamma$ , etc.).

## 2.4.3 Damping coefficient vs. diameter of microbubbles

Figure 2.2 and Figure 2.3 depict the relationship between the various damping coefficients: thermal conductivity, viscosity, and reradiation versus microbubble radius for the case of a free bubble ( $S_p = 0$  N/m) and an encapsulated bubble ( $S_p = 10$  N/m) (see Equations (2.14), (2.15), and (2.16)). There are some differences between the two sets of graphs, which can be attributed to the value used for the ratio of specific heats of the encapsulated gas,  $\gamma$ . De Jong et al. [13] conducted their experiments with Alunex, which has an air gas core ( $\gamma = 1.4$ ), whereas our experiments were conducted with Definity, which has an octofluoropropane gas core ( $\gamma = 1.06$ ). Damping coefficients were calculated at the resonant frequency of the bubbles with the polytropic coefficient,  $b^{-1}$ , being approximated by the ratio of specific heats,  $\gamma$ . Even though different values for the ratio of specific heats were used, good agreement between simulation and literature results further support the validity of our code.

#### 2.4.4 Scattering cross section vs. frequency

Figure 2.4a and Figure 2.4b illustrate the relationship between the scattering cross section (see Equation (2.2)) and frequency. As predicted by de Jong et al. [13], encapsulation (i.e., cases where the shell parameter,  $S_p$ , and shell friction,  $S_f$ , terms are non-zero positive values) causes an increase in the resonant frequency and a slight decrease in the scattering amplitude of the microbubble. The increase in resonant frequency occurs because the presence of the shell increases the restoring force that causes the bubble to tend to converge back to its state of equilibrium. The slight decrease in scattering amplitude arises due to the extra energy loss via internal friction within the shell [3]. Good correlation between simulation results and literature values further substantiate the accuracy of our theoretical backscatter cross section code.

#### 2.5 Theoretical Backscatter Cross Section vs. Frequency

Figure 2.5 illustrates the relationship between the backscatter cross section as described in Equation (2.2) versus frequency. A Gaussian distribution of microbubble sizes with a mean radius of  $1.32 \mu\text{m}$ , variance of  $0.477 \mu\text{m}$ , and concentration of  $1.737 \times 10^6$  microspheres/mL was used to construct the backscatter cross section models observed in Figure 2.5. The shell parameter value was varied ( $S_p = 1.7, 5, 7,$  and  $9.5 \text{ N/m}$ ) to assess its effect on the backscatter cross section. According to Goertz et al. [7], the shell parameter values,  $S_p$ , for Definity and Albutex microbubbles are  $1.7 \text{ N/m}$  and  $9.5 \text{ N/m}$ , respectively. As mentioned before, increasing the shell parameter results in an increase in the microbubble's restoring force and therefore its resonant frequency. This explains the shift to high resonant frequencies with increasing values of the shell parameter. Simulation results, however, also reveal a broadening in the bandwidth of the resonance peak with increasing  $S_p$ . This phenomenon can be explained using spring mechanics. Just as a spring has a lower quality factor (i.e., broader bandwidth) when its restoring force is larger, a microbubble, having a restoring force proportional to  $S_p$ , will similarly have a broader bandwidth as  $S_p$  increases.

Due to quantization of the size distribution of bubbles, we observed a ripple effect in the theoretical backscatter cross section vs. frequency plots. A continuous size distribution of bubbles would have produced a smoother plot.

## 2.6 Measured Backscatter Cross Section

In Section 2.2, we defined the backscatter cross section as the fraction of energy the scatterer extracts from a sound beam of  $1 \text{ m}^2$  cross section [10]. In mathematical terms, assuming incoherent scatter, the definition above yields:

$$N\sigma_{bs} = \frac{|V_S(f)|^2}{|V_I(f)|^2} \quad (2.18)$$

where  $N$  is the number of scatterers corresponding to the backscattered signal being analyzed for one particular size of scatterers,  $\sigma_{bs}$  is the backscatter cross section for a single scatterer,  $|V_S(f)|^2$  is the power spectrum of the backscattered signal from a UCA mixture as a function of frequency and  $|V_I(f)|^2$  is the power spectrum of the sound incident on the scattering volume as a function of frequency.  $|V_S(f)|^2$  is obtained by taking the magnitude squared of the Fourier transform of a gated segment of the backscattered ultrasound signal from the microbubbles.

The incident sound is assumed to be near the focus and axis of a weakly focused transducer so that the field can be approximated as a plane wave. The power spectrum of the sound incident on the scattering volume can be characterized as

$$|V_I(f)|^2 = \frac{|V_R(f)|^2}{\Gamma^2} \quad (2.19)$$

where  $|V_R(f)|^2$  is the power spectrum of backscattered signal from a planar reflector (i.e., Plexiglas) as a function of frequency, and  $\Gamma$  is the reflection coefficient of the reflector. When Equation (2.19) is substituted into Equation (2.18), we obtain the total normalized backscatter cross section from a population of scatterers of a single size. To account for a distribution of scatterer sizes, we simply sum the backscatter cross section contributions from each scatterer size population, giving

$$\sum_{i=1}^N \sigma_{bs}(r_i, f) = \frac{\Gamma^2 |V_S(f)|^2}{|V_R(f)|^2}. \quad (2.20)$$

Equation (2.20) describes the relationship between the theoretical (left side of Equation (2.20)) and measured (right side of Equation (2.20)) backscatter cross section.

## 2.7 Attenuation Coefficient

Attenuation, which results in the reduction in a signal's intensity, arises from (1) absorption (i.e., the conversion of acoustic energy into thermal energy) and (2) scattering (i.e., reradiation of incident acoustic energy into all directions) [10]. In the in vitro studies, the main source of absorption and scattering is the contrast agent, with attenuation increasing proportionately to the concentration of microbubbles. Because of attenuation, a phenomenon called *UCA shadowing* occurs in which the microbubbles at the surface closest to the transducer attenuate the acoustic signal, reducing the intensity of the signal with depth into the sample (see Figure 2.6). The consequence of this phenomenon is an underestimation of the bubble concentration because signal power with depth is decreased. To compensate for this underestimation, an attenuation correction factor,  $A(\alpha(\omega), c\tau)$ , was incorporated into the postprocessing code [18],

$$A(\alpha(\omega), c\tau) = \frac{4\alpha * c\tau}{1 - e^{-4\alpha * c\tau}} \quad (2.21)$$

where  $\alpha(\omega)$  is the frequency dependent attenuation of the UCA mixture and  $c\tau$  is the length of the gate used to analyze the ultrasound backscattered signal.

Values for the frequency dependent attenuation,  $\alpha(\omega)$ , through a cloud of microbubbles were estimated from results obtained by Chatterjee et al. (refer to Figure 2.7, Table 2.3 and Table 2.4) [19]. Using the UCA concentration results obtained from the hemacytometer analysis, attenuation values at various frequencies were extrapolated from Figure 2.7. These values were then used to compensate for frequency-dependent attenuation of the backscattered power spectrum to provide accurate estimates of the UCA concentration.

## 2.8 Figures

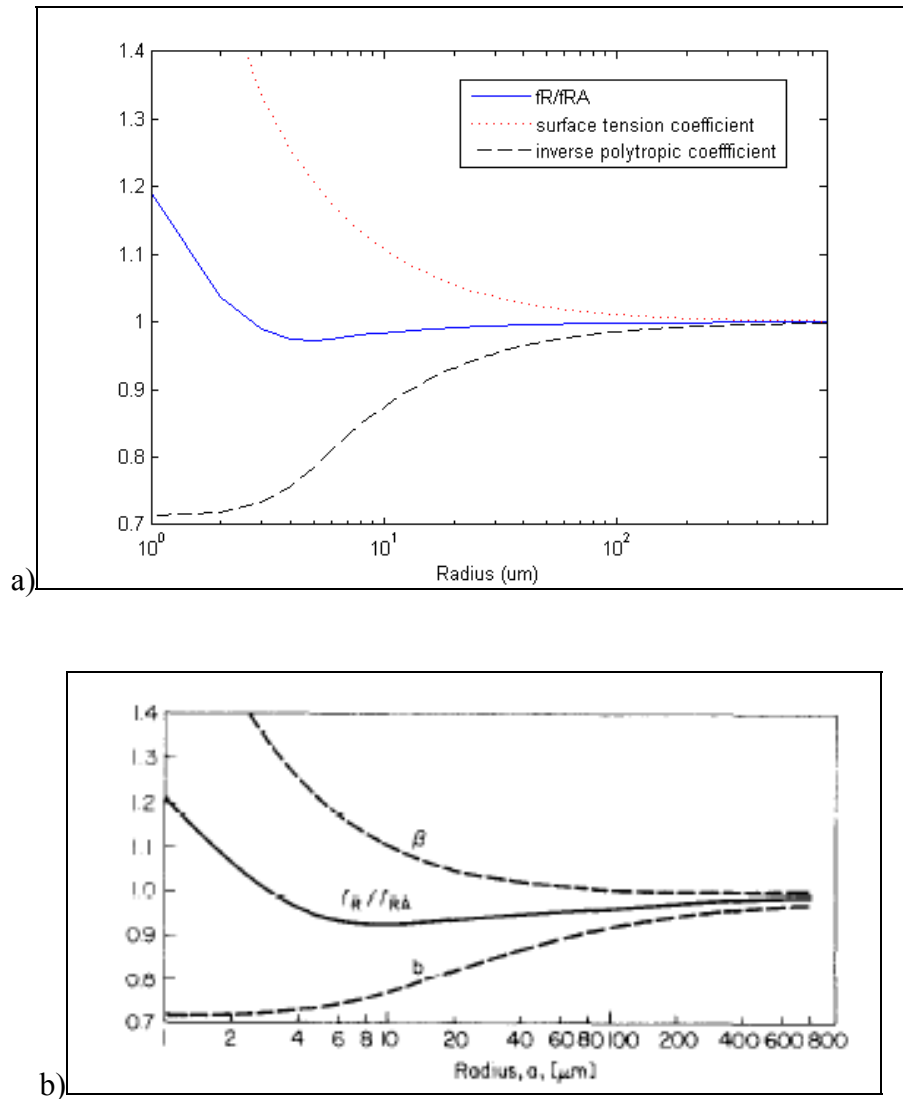


Figure 2.1 Inverse polytropic coefficient and surface tension coefficient vs. radius of an air bubble in water where  $\beta$  is the surface tension coefficient,  $b$  is the inverse polytropic coefficient, and  $f_R/f_{RA}$  is  $(\beta b)^{1/2}$  derived using (a) our computer code and (b) results obtained by Medwin [12].

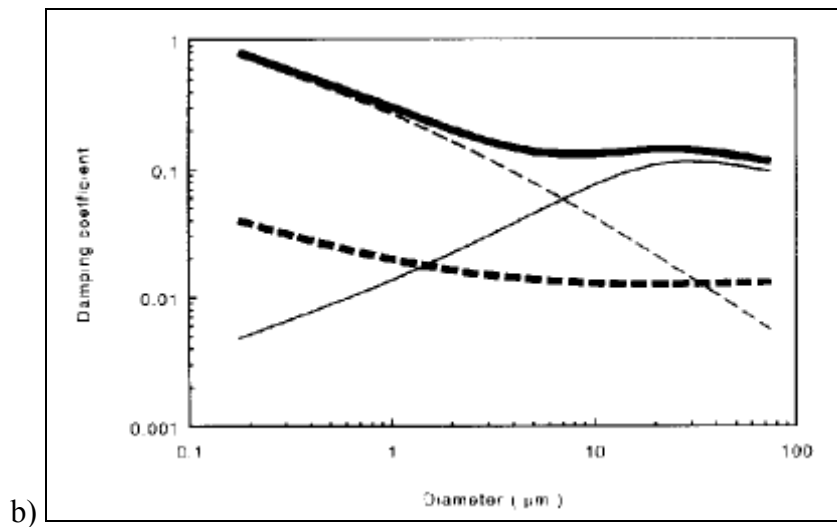
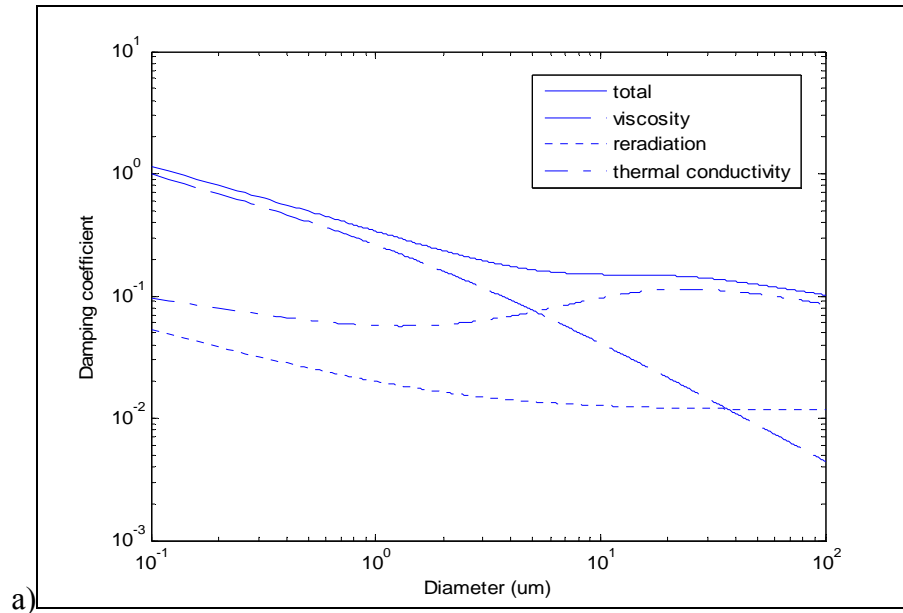


Figure 2.2 Damping coefficient vs. diameter for air bubbles ( $S_p = 0$  N/m) derived using (a) our computer code and (b) results obtained from de Jong et al. [13].

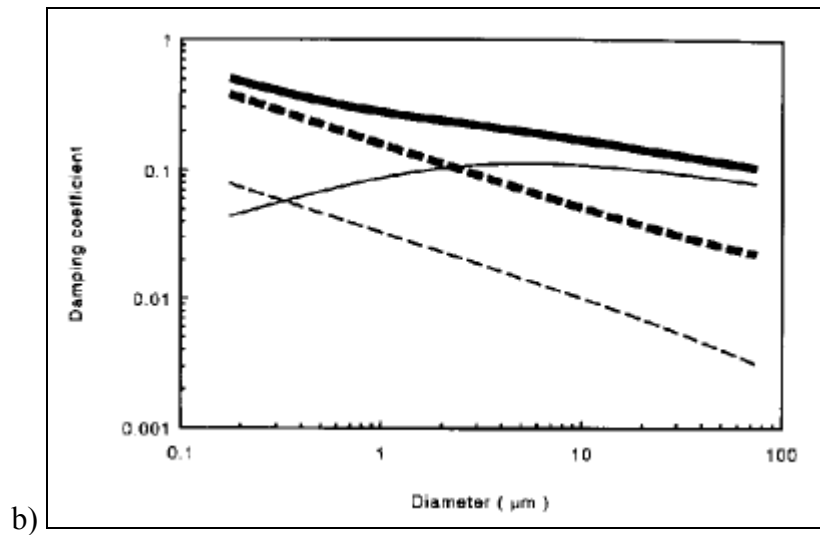
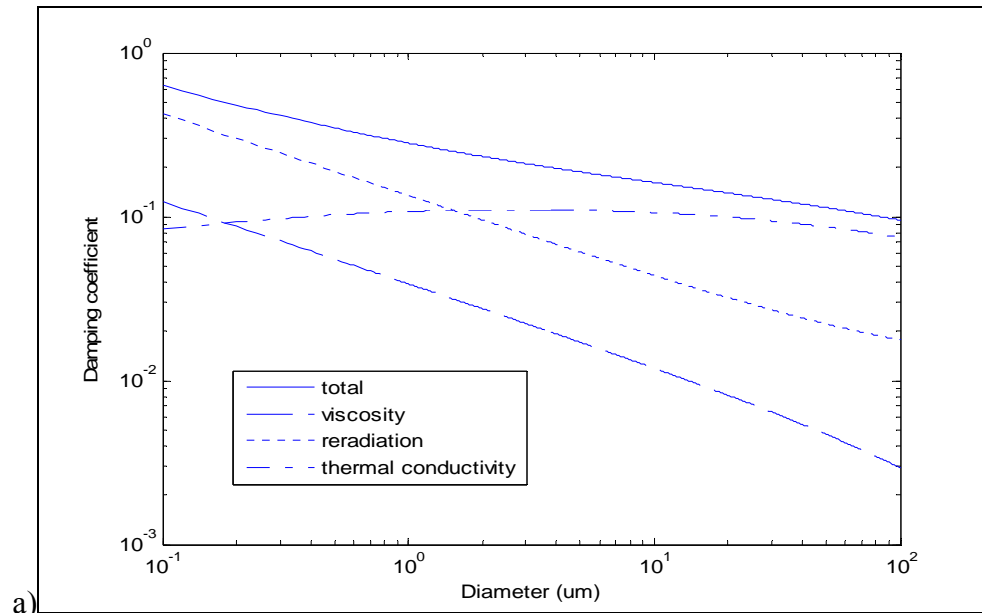


Figure 2.3 Damping coefficient vs. diameter for bubbles with  $S_p = 10$  N/m derived using (a) our own computer code and (b) results obtained from de Jong et al. [13].

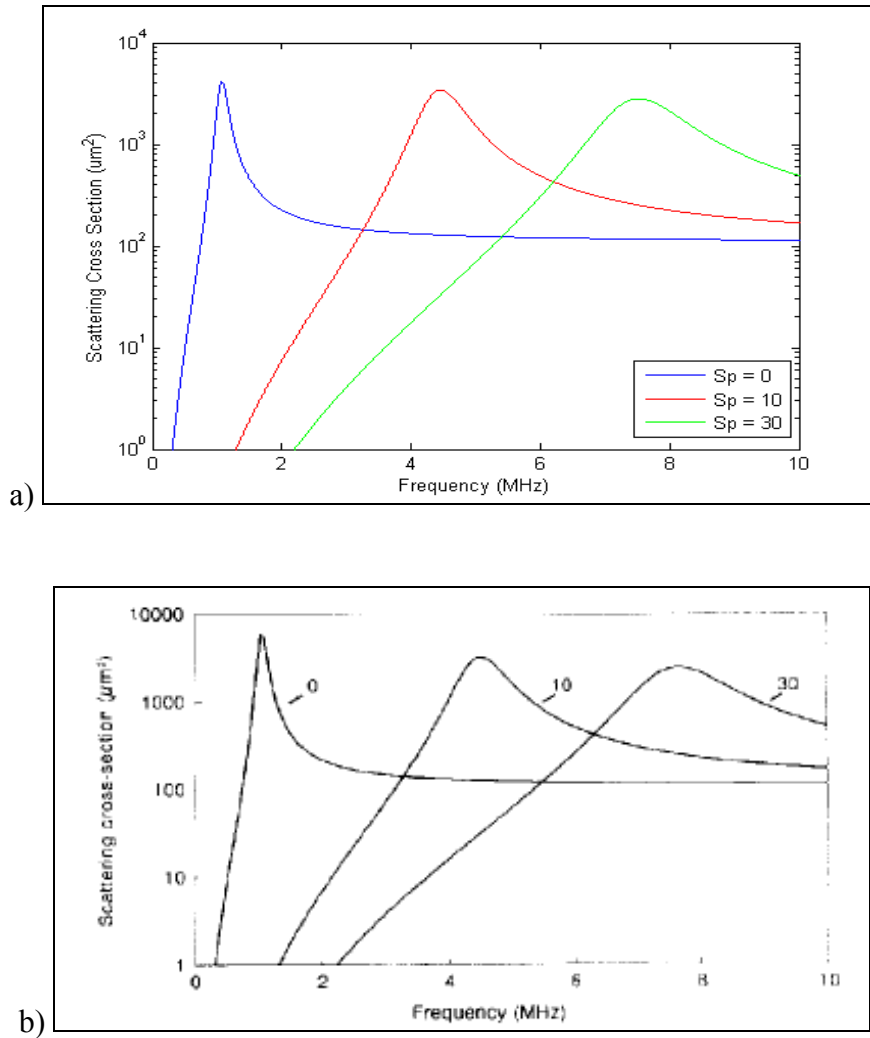
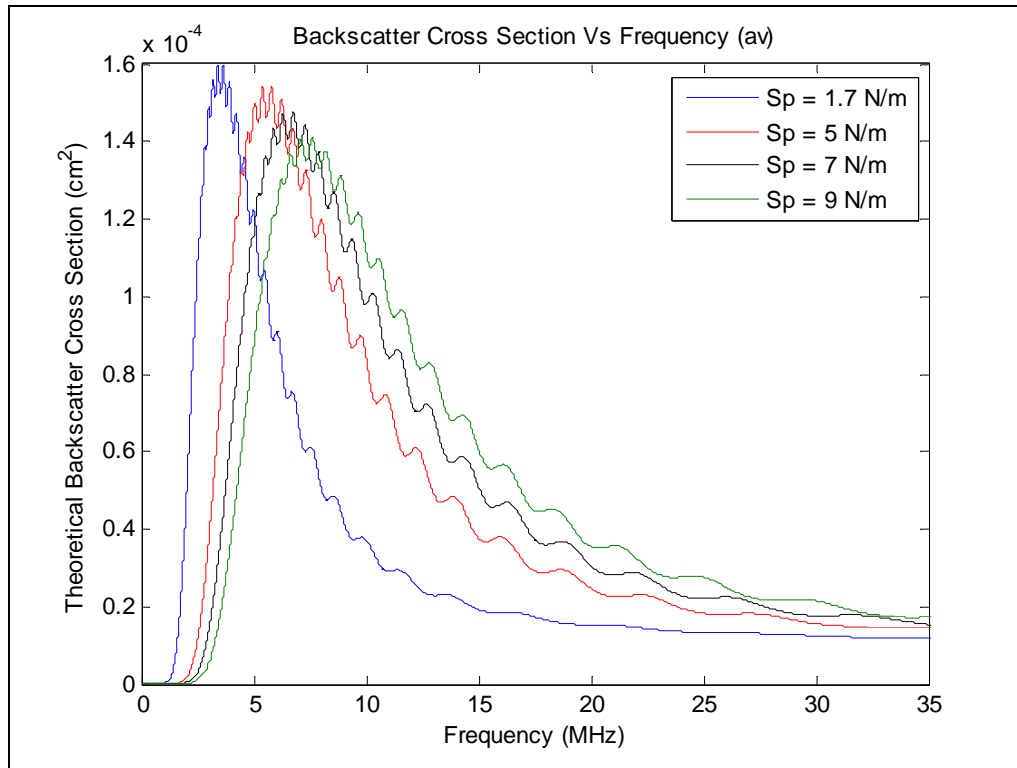


Figure 2.4 Theoretical scattering cross section vs. frequency for a 6 μm diameter bubble at shell parameters of 0, 10 and 30 N/m derived using (a) our computer code and (b) results obtained from de Jong et al. [13].



**Figure 2.5 Theoretical backscatter cross section vs. frequency for different shell parameter values (1.7, 5, 7 and 9.5 N/m).**

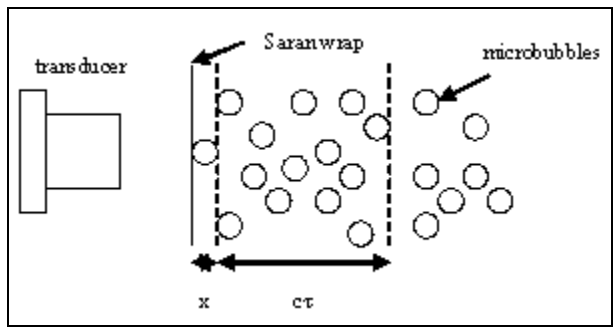


Figure 2.6 Diagram describing attenuation correction factor.

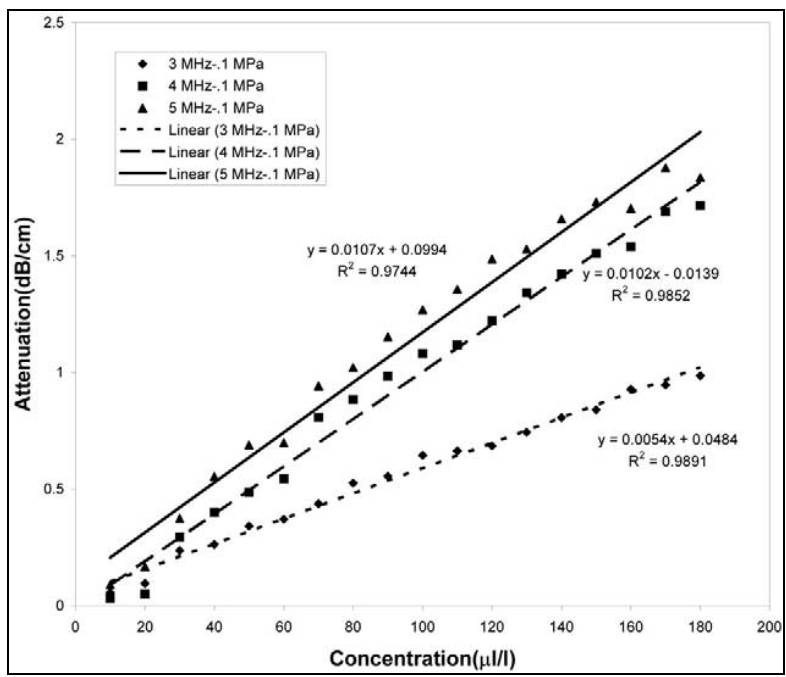


Figure 2.7 Attenuation results obtained by Chatterjee et al. [19].

## 2.9 Tables

**Table 2.1 Table of parameters for Definity microbubbles.**

<i>Symbol</i>	<i>Description</i>	<i>Value</i>
$\gamma$	Ratio of specific heats for octofluoropropane	1.06
$\rho$	Water density	1.03 g/cm <sup>3</sup>
$P_0$	Ambient pressure	1.01325e5 Pa
$\rho_{gA}$	Density of free gas	1.29e-3 g/cm <sup>3</sup>
$C_{pg}$	Specific heat at constant pressure of gas	0.24 cal/gm
$K_g$	Thermal conductivity of gas	5.6e-5 cal/cm/s/°C
$\tau$	Surface tension	75 dyne/cm
$\eta$	Shear viscosity of liquid	0.01 gm/cm/s
$S_f$	Shell friction	0.015e-6 kg/s
$S_p$	Shell parameter	1.7 N/m

**Table 2.2 Resonance frequency (MHz) of UCAs as a function of bubble diameter and shell parameter derived using (a) our computer code and (b) results obtained from de Jong et al. [13].**

a)

Bubble Diameter ( $\mu\text{m}$ )	Shell parameter (N/m)			
	0	5	10	20
1	9.43	45.3	63.4	89.2
3	2.35	8.85	12.3	17.2
5	1.29	4.17	5.76	8.04
8	0.76	2.1	2.88	3.99
10	0.598	1.52	2.07	2.87
20	0.286	0.57	0.76	1.03

b)

Bubble diameter ( $\mu\text{m}$ )	Shell parameter			
	0	5	10	20
1	9.5	45.4	64.0	90.3
3	2.4	8.9	12.4	17.5
5	1.3	4.2	5.9	8.2
8	0.8	2.1	2.9	4.1
10	0.6	1.5	2.1	2.9
20	0.3	0.6	0.8	1.1

**Table 2.3 Attenuation values at 3 MHz interpolated from curves by Chatterjee et al. [19].**

	<b>UCA Concentration (<math>\mu\text{L/L}</math>)</b>	<b>Attenuation (dB/cm)</b>	<b>Attenuation (Np/cm)</b>
0.1x	38.14	0.254	0.0292
1x	115.82	0.674	0.0776
2x	183.97	1.042	0.1199

**Table 2.4 Attenuation values at 6 MHz interpolated from curves by Chatterjee et al. [19].**

	<b>UCA Concentration (<math>\mu\text{L/L}</math>)</b>	<b>Attenuation (dB/cm)</b>	<b>Attenuation (Np/cm)</b>
0.1x	38.14	0.507	0.0584
1x	115.82	1.339	0.1541
2x	183.97	2.068	0.2381

## CHAPTER 3: METHODS AND MATERIALS

### 3.1 Properties of Transducers

Four weakly focused transducers ( $f/3$  and  $f/4$ ) centered at 3 MHz, 6 MHz, 10 MHz and 20 MHz were used to characterize the frequency-dependent behavior of the UCAs. Table 3.1 documents some of the more important properties of these transducers (e.g. -6 dB bandwidth, F-number, aperture diameter, etc.).

The peak rarefactional acoustic pressure at the focus of each transducer was measured (see Table 3.2) to ensure that the induced pressures did not exceed the cavitation threshold ( $\sim 1$  MPa) (i.e., the point at which a bubble in liquid rapidly collapses and produces a shock wave). Each transducer was connected to a Panametrics 5800 pulser-receiver and positioned so that its focus was targeted directly onto the sensing element of a Marconi M3 PVDF membrane hydrophone (Coswell Tech, Northants, UK). Different input energy settings on the Panametrics 5800 were used to find the appropriate rarefactional pressure level. To convert the measured voltage to a pressure value, a conversion ratio of 0.043 V/MPa was used.

In the perfusion phantom experiments, because the acoustic signal had to propagate through 1/16 inch of silicon tubing, there was naturally an attenuation of the signal and subsequent reduction in peak rarefaction pressure at the focus of the transducer (see Table 3.3).

In order to ensure that the UCAs were not being destroyed by the ultrasonic fields, the peak rarefactional pressure values at the focus of the transducers using the final experimental settings were estimated (bolded values in Table 3.2 and Table 3.3). Estimates of the peak rarefactional pressure were measured and are listed in Table 3.2 and Table 3.3. By comparing the bolded values to the peak rarefactional pressure that would cause a microbubble to undergo inertial cavitation in Figure 3.1 [20], we were able to confirm that at our energy settings, the pressure levels used with the 3 MHz and 6 MHz transducers were below the threshold of collapse for single microbubbles. No data was available for the inertial cavitation thresholds of Definity microbubbles at 10 MHz and 20 MHz. Other studies conducted by Shi et al. [21] observed inertial cavitation

events occurring at pressures exceeding 1.6 MPa at 2.5 MHz (0.4-1.0 in mechanical index). However, Sboros et al. [22] and Dayton et al. [6] have observed that at pressures even as low 0.6 MPa when using a 3 MHz transducer, ultrasonic waves can induce lesions in the microbubble shell by which gas can escape. Fortunately, the results of these studies have also indicated that this phenomenon almost solely occurs with albumin-shelled bubbles. Because of the flexibility of its shell, Dayton et al. [6] observed that phospholipid-shelled bubbles such as Definity microbubbles exhibit more robustness in the presence of an acoustic field. Therefore, we assumed the probability of an inertial cavitation event occurring to be minimal at the pressure levels used for all frequencies.

### **3.2 In Vitro Experiments**

Experiments were conducted to test the hypothesis that ultrasound backscatter could be used to estimate the instantaneous concentration of microbubbles. The first set of experiments used a simplified in vitro system to assess the feasibility of the technique and to identify any potential roadblocks to in vivo implementation. The first sets of experiments were conducted with UCAs mixed in a beaker of fluid. The second sets of experiments increased the complexity of the system by introducing flow. The introduction of a flow in the system would more closely mimic the bloodstream conditions, but with in vitro experiments, the conditions could be better quantified and controlled. The experiments in the flow phantom would also enable the identification of potential in vivo implementation issues. Finally, after demonstrating success in the in vitro studies, experiments were conducted in vivo.

#### **3.2.1 Beaker experiments**

Initial in vitro experiments were conducted within a 250 mL beaker (see Figure 3.2). A known concentration, either 0.1x, 1x, or 2x the normal dosage of Definity (i.e.,  $\sim 8 \times 10^{-5}$  mL of Definity per mL), was introduced into 250 mL of degassed water and continuously but gently homogenized throughout the experiment with a magnetic stir bar. The stir bar ensured that the concentration of UCAs at the focus of the transducer was constantly replenished. Five hundred snapshots of the backscattered signal from the microbubbles were taken over a period of 30 to 50 min in intervals of 5 min. Results were

divided into two groups: (1) “After Vialmix” and (2) “Out of Refrigerator.” The “After Vialmix” samples were samples of Definity used immediately after activation while the “Out of Refrigerator” samples represent Definity used after having been stored in a refrigerator at 6°C a few hours after Vialmix activation.

Either a Panametrics 5800 or 5900 pulser-receiver (Panametrics Inc., Waltham, MA, USA) was used to produce the incident acoustic wave through pulsed excitation. Refer to Table 3.4 for the settings used to drive the four different transducers. For all four cases, the transducer was set to transmit and receive (i.e., pulse-echo mode).

The received signal (i.e., the backscattered signal) was digitized and imaged on an oscilloscope. Five hundred snapshots of the backscattered signal were obtained every 5 min and stored onto a PC for postprocessing and analysis.

For all in vitro experiments, an estimate of the noise was obtained by acquiring snapshots of the signal in a region corresponding to degassed water only. In addition, a reference scan with a Plexiglas reflector was acquired (see Figure 3.3 for reference scan setup) in order to normalize the backscattered power spectrum. The normalization eliminated the effects of the equipment and noise produced by the experimental setup, isolating the backscatter power due only to the UCAs. A parameter describing the magnitude of the backscatter power spectrum was obtained by averaging the power spectrum over the -6 dB bandwidth of the active transducer.

### **3.2.2 Perfusion phantom experiments**

In vitro experiments were also conducted within a perfusion phantom to simulate the cardiovascular system. These experiments allowed us to examine the concentration of UCAs within a moving system. The perfusion phantom consisted of a peristaltic pump (Masterflex Variable Speed Economy Console Drive) used to propel the mixture of UCAs throughout the system (see Figure 3.4), a measuring site, and mixing reservoir [8]. Because the UCAs were moving, at certain incident angles it was possible that a Doppler shift could be observed in the backscatter. However, because the transducer was positioned perpendicular to the flow of UCAs, the Doppler shift was minimized. Even if the transducer was angled with respect to the flow of UCAs, the expected Doppler shift (see Equation (3.1)) at 45° off the axis perpendicular to the flow of UCAs would be 1.191

kHz for the 6 MHz transducer, or 0.02% of the active frequency. This shift in frequency would be insignificant and was considered to be negligible. The Doppler shift was estimated by

$$\Delta f = \frac{2Uf \cos \theta}{c} \quad (3.1)$$

where  $U$  is the velocity of mixture within the perfusion phantom,  $\theta$  is the angle between the transducer and direction of UCA mixture flow,  $f$  is the frequency of the active transducer, and  $c$  is the speed of sound in water.

The measuring site is located where the beam of the transducer intersects with the precision silicone tubing (Masterflex L/S 17 with an inner diameter of ¼ inch). The mixing reservoir follows the same setup depicted in Figure 3.2, except the beaker is not covered with Saran Wrap and is not surrounded by degassed water. Different concentrations of UCAs, either 0.1x, 1x, or 2x the normal dosage of Definity, were introduced into the mixing reservoir, allowed to homogenize for a few seconds, and then pumped through the perfusion phantom at a flow rate of approximately 400 mL/min, which is the average blood flow rate in the human body.

Procedures for data acquisition are the same as outlined in Chapter 3.2.1. However, because of the ~20 dB attenuation through the silicone tubing, the energy input from the Panametrics 5800 had to be increased from 12.5  $\mu$ J to 100  $\mu$ J for the 3 MHz and 6 MHz transducers. The 10 MHz and 20 MHz transducers were not used in the perfusion phantom experiments because excessive attenuation through the silicone tubing made it difficult to distinguish the backscattered signal from the noise floor (i.e., poor signal-to-noise ratio).

As before, the noise floor was subtracted from UCA backscatter measurements in the power spectral domain and then the result was normalized by the power spectrum of the reference. A parameter describing the magnitude of the backscatter power spectrum was obtained by averaging the power spectrum over the -6 dB bandwidth of the active transducer.

### 3.3 In Vivo Experiments

In vivo experiments were conducted on New Zealand white rabbits (Myrtle's Rabbitry, Thompson Station, TN, USA). Rabbits were weighed before each experiment ( $4.85 \pm 0.98$  kg) and anesthetized with ketamine hydrochloride (50 mg/kg) and xylazine (10.0 mg/kg) administered subcutaneously. Once anesthetized, the rabbits were placed under right lateral recumbency on top of a thick insulating paper barrier to minimize heat loss.

Hair over the dorsal surface of the right auricular artery was removed using an electric clipper followed by a depilatory agent (Nair, Carter Wallace, Inc., New York, NY, USA). To maximize acoustic transmission, mineral oil was applied at the interface of the depilated skin and stand-off tank. A balloon filled with degassed water was placed on the distal side of the ear to absorb the sound waves and minimize reflections from the distal side of the ear [23] (see Figure 3.5).

A 20 MHz transducer (see Table 3.1 for transducer properties) was positioned to image a 2.5 mm by 4 mm cross section of the central auricular artery. The central auricular artery was selected in these experiments for its size and similarity in anatomic structure to the human coronary artery. Before a bolus of Definity microbubbles (10  $\mu$ L/kg) was injected into the lateral saphenous vein, a B-mode image of the auricular artery was acquired to locate the auricular artery (see Figure 3.6). The transducer was then positioned so that its focus was directly centered inside the artery. For use as a reference, 1000 baseline snapshots taken over a time span of ~4 min in the absence of UCAs were acquired. Three different concentrations of Definity – 1x, 2x, and 5x the normal dose – were administered. After each administration, 1000 snapshots of the central auricular artery were obtained, and the Definity was allowed sufficient time to exit the body. According to Droste, >75% of the UCAs are removed from the body via the lungs after 11 min [24]. Figure 3.5 illustrates the setup used in the in vivo experiments and Figure 3.6 is a B-mode image of the central auricular artery in the absence of contrast agents. Because blood is a weak scatterer of ultrasound over the frequency range of 3 to 20 MHz, the central auricular artery can be identified by the dark circular region in Figure 3.6.

### 3.4 Optical Estimation of Microbubble Concentration

Optical estimates of microbubble concentration were obtained using a hemacytometer (see Figure 3.7) to compare against the U/S estimates. Concentrations of 0.1x, 1x and 2x the normal dosage of Definity were prepared and the samples quantified under a light microscope. For each count, at least 100 microbubbles within the laser-etched  $0.04 \text{ mm}^2$  (see Figure 3.8 and Figure 3.9) squares were tallied, and then the appropriate dilution and correction factors were employed to obtain the total microbubble count (see Equation (3.2)). Since the area bounded by the lines is known and the depth of the chamber is also known, it is possible to count the number of particles in a specific volume of fluid. In a typical 1x concentration count, we tallied approximately 110 microbubbles in sixteen  $0.04 \text{ mm}^2$  squares. Using Equation (3.2), where  $C$  is the correction factor which converts  $1 \text{ mm}^3$  to  $1 \text{ mL}$  (i.e.,  $10^4$ ), we calculated the UCA concentration to be  $171.875 \times 10^4$  bubbles/mL.

$$\text{Bubble count} / ((\# \text{ of } 1/25 \text{ mm}^2 \text{ squares})/25) * C = \text{bubbles/mL} \quad (3.2)$$

### 3.5 Estimating UCA Size Distribution

Samples of the Definity mixtures were occasionally extracted and examined under a fluorescence microscope (Zeiss Axiovert 200M Microscope). These samples were magnified 63x and exposed to a bright field. Images were acquired and a size distribution of the bubbles was obtained using two different MATLAB programs. One program analyzed the images in the spatial domain and the other in the frequency domain. Results from these two programs were compared against each other for verification purposes. The reason for estimating the size distribution is that the backscattered power is highly sensitive to the size of the scatterer, i.e, it is proportional to the size of the scatterer to the sixth power.

Dayton et al. observed, acoustically and optically, that UCAs dissolve over time [6]. However, we hypothesized that larger bubbles were dissolving more rapidly than smaller ones. This was one of the motivations behind obtaining size distributions of Definity microbubbles over a period of time. In addition, estimates of the size distribution could be fed into the scattering models to help predict the scattering due to UCAs. To do

this, samples of the UCA mixture in a 250 mL beaker were extracted every 5 min. The UCA mixture in the beaker was constantly but gently stirred to keep the solution of UCAs uniformly and randomly mixed in the water. The magnetic stirrer continued to homogenize the mixture as samples were being extracted. After extraction, two methods were used to estimate the size distribution of the UCAs: a spatial domain analysis technique and a Fourier domain analysis technique.

### **3.5.1 Image analysis in the spatial domain**

Images of the microbubbles were captured with a camera (512 x 512 pixel array), converted to a JPEG file, and transferred to a computer for processing with a custom made code (MATLAB). Given an image of microbubbles, the image processing code first convolves a 2-D mask over the entire image space (see Figure 3.10 and Figure 3.11).

Wherever there is a circular structure surrounded by a black ring in the image, the convolved image peaks in value. By setting a threshold on the convolved image and equating all pixels within the convolved image with values above the threshold to one and all pixels with values below that threshold to zero, the convolved image essentially becomes a binary image that marks the position of all the circular structures in the image file (see Figure 3.12). Figure 3.12 also illustrates that these position markers are size dependent and therefore were used to obtain size estimates.

Because the diameter of Definity microbubbles ranges from 1.1 to 3.3  $\mu\text{m}$ , multiple 2-D masks of differing widths were used to convolve over images containing UCAs. Analysis in the spatial domain generated a distribution of the UCA sizes as well as mean, median, and standard deviation of the population (see Figure 3.13). These distribution plots could then be fed back into the models to predict the backscatter from a population of microbubbles.

### **3.5.2 Image analysis in the frequency domain**

Analysis in the frequency domain consisted of first converting the input image into a gray-scale bitmap. A 2-D Fourier transform (FT) was then performed on the gray-scale bitmap, resulting in a weighted 2-D jinc function (see Figure 3.14). From the 2-D jinc function, a 1-D horizontal slice was extracted (see Figure 3.15). An estimate of the

average microbubble diameter was obtained by fitting a jinc function to the 1-D horizontal slice (see Figure 3.15) and analyzing the width of the jinc function's main lobe. The best-fit jinc function could then be related to an average size of the microbubbles for predicting the ultrasonic backscatter from the bubble population.

### **3.5.3 Test of image processing accuracy with latex spheres**

The accuracy of the sizing code was tested by processing images of latex spheres of known diameter ( $\mu\text{m}$ ) with a small variance in size ( $1.025 \pm 0.01 \mu\text{m}$ ) (see Figure 3.16). Estimates of the latex sphere sizes using the spatial domain analysis were  $1.025 \pm 0.188 \mu\text{m}$  (see Table 3.5).

According to the product label, the diameter of the latex spheres should only vary by  $\pm 0.01 \mu\text{m}$ . Our results, however, indicated a standard deviation of  $\pm 0.188 \mu\text{m}$ , almost 20 times the quoted standard deviation. Tests using the code with images of single latex spheres that were in and out of focus produced standard deviations close to  $\pm 0.188 \mu\text{m}$ , suggesting that the source of variation is characteristic of the imaging device (see Figure 3.17). More specifically, even though the variation in sizes may actually be approximately  $0.01 \mu\text{m}$ , we measured a large variance because some spheres were in focus and others were out of focus (see Table 3.6). The success of the latex sphere sizing suggests that the results yield an accurate and precise estimate of the distribution of spheres. However, the estimated variance of the particle sizes may be larger than the true variance of the particle sizes because of the focusing effect. With a population of spheres with a larger distribution of sizes, this should not significantly affect the estimate of the distribution of scatterer sizes.

## **3.6 Monte Carlo Simulation**

A Monte Carlo simulation is a class of computational algorithms that rely on repeated random sampling. In this study, the Monte Carlo simulation was used to extract estimates for the mean microbubble radius, variance of microbubble radius assuming a Gaussian distribution of radii, and concentration. This was accomplished by repeatedly fitting a theoretical backscatter model to measured data by repeatedly and randomly choosing different values for microbubble radius, variance, and concentration to update

the theoretical model. Values of the mean microbubble radius, radius variance, and concentration of microbubbles were used to define a Gaussian distribution of microbubble sizes (refer to Figure 3.18). This Gaussian distribution was then used to construct the theoretical backscatter cross section model. At each iteration of the simulation, the mean squared error (MSE) between the measured and theoretical backscatter cross section was calculated (refer to Figure 3.19). Current values for the mean radius, variance of the radius, and UCA concentration were stored as the optimum values every time a new minimum MSE was attained. The Monte Carlo simulation continued iterating until either the number of iterations reached a user-defined maximum of 10 000 iterations or the MSE between the theoretical and measured cross sections was less than  $1.5 \times 10^{-3}$ . Values for the mean radius, variance of the radius, and UCA concentration obtained through simulations were compared against size distribution measurements obtained through hemacytometer and image processing techniques to check the validity of the theoretical backscatter model. Good correlation between theory and measured data in Figure 3.19 indicates that the Gaussian distribution of microbubble sizes can be used to accurately predict the frequency-dependent behavior of the backscatter from Definity microbubbles in vitro.

### 3.7 Figures

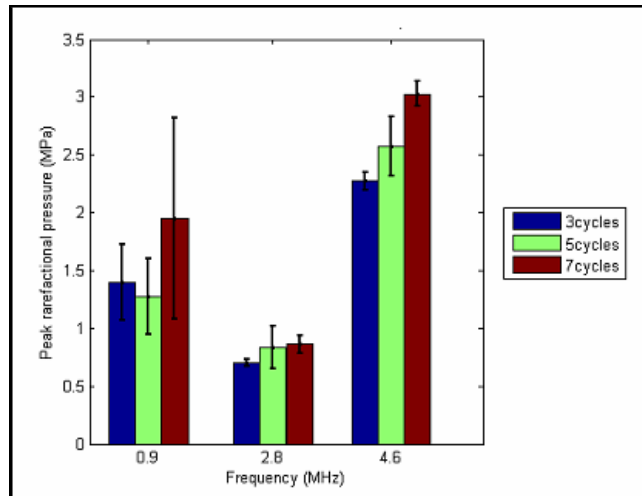


Figure 3.1 Peak rarefactual pressure at which inertial cavitation of Definity® microbubbles occurs obtained by Haak et al. [20].

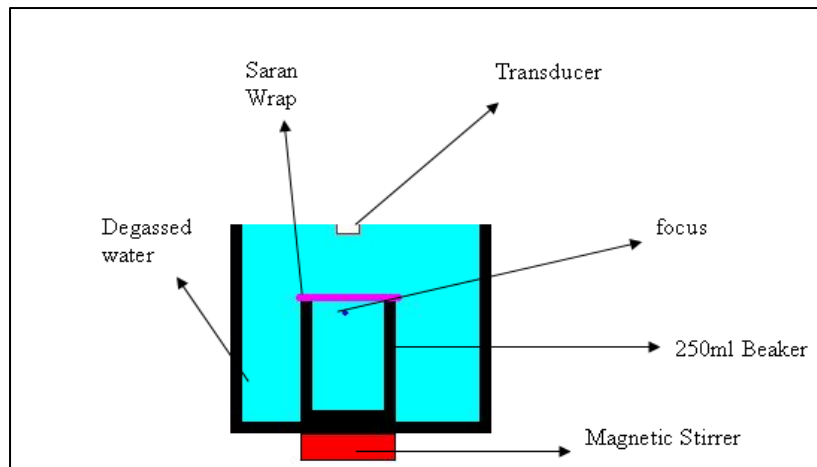


Figure 3.2 Diagram of experimental setup.

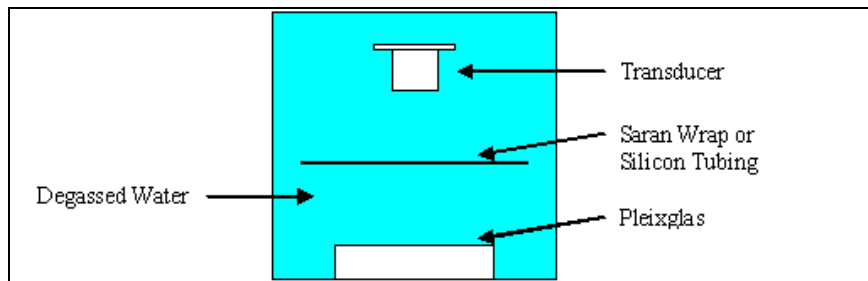
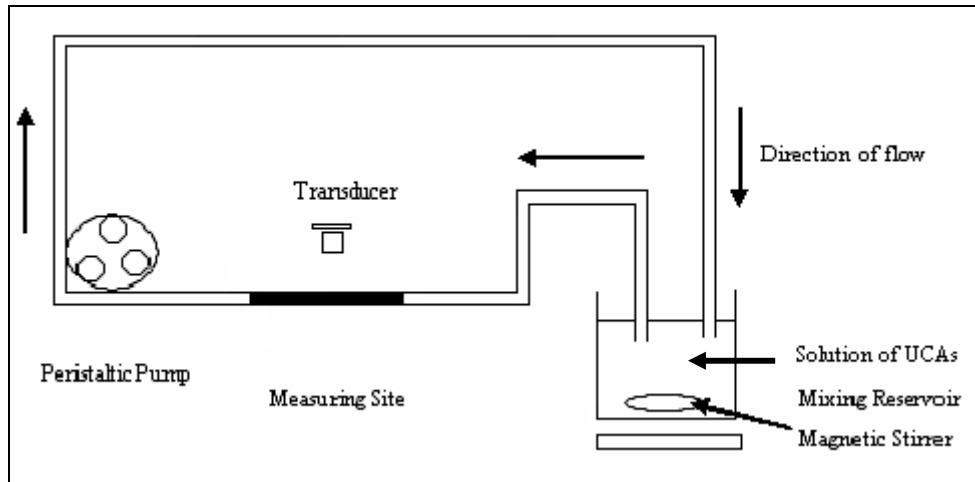


Figure 3.3 Diagram of reference scan setup.



**Figure 3.4 Diagram of perfusion phantom.**

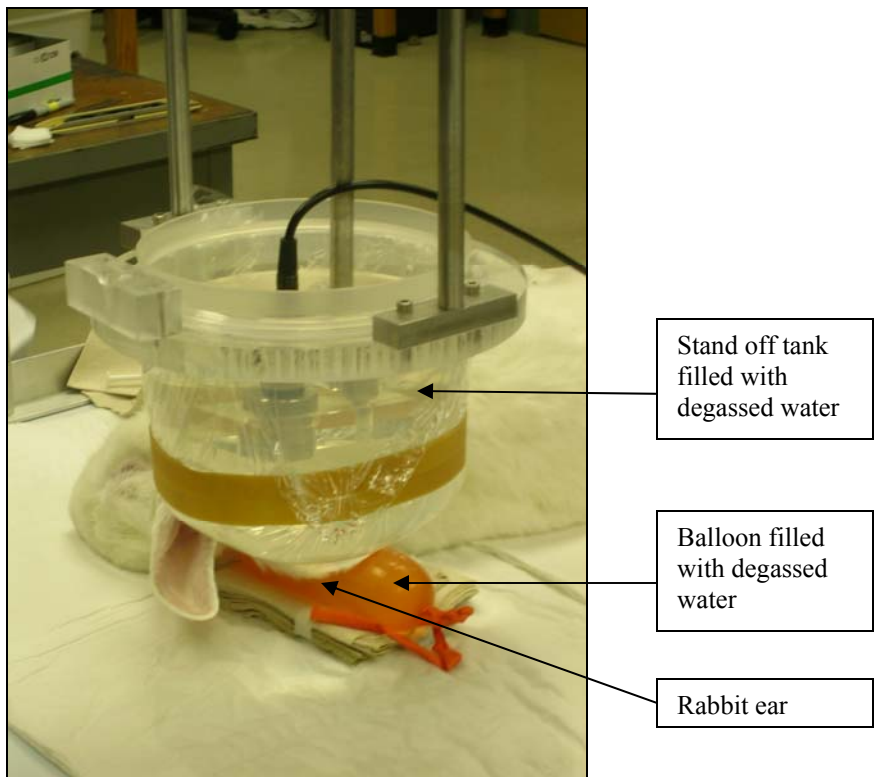
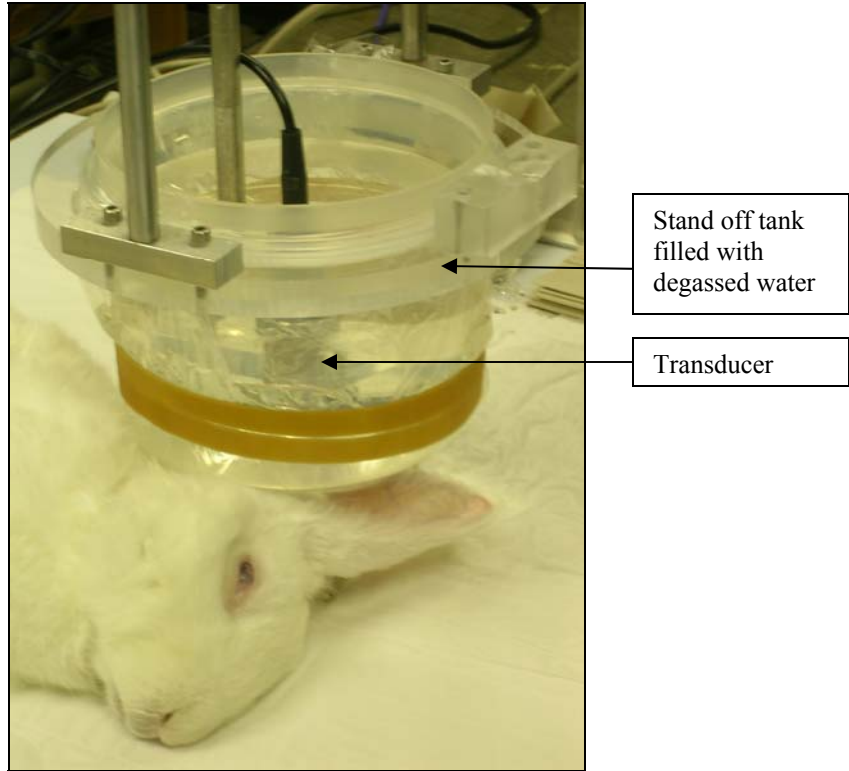
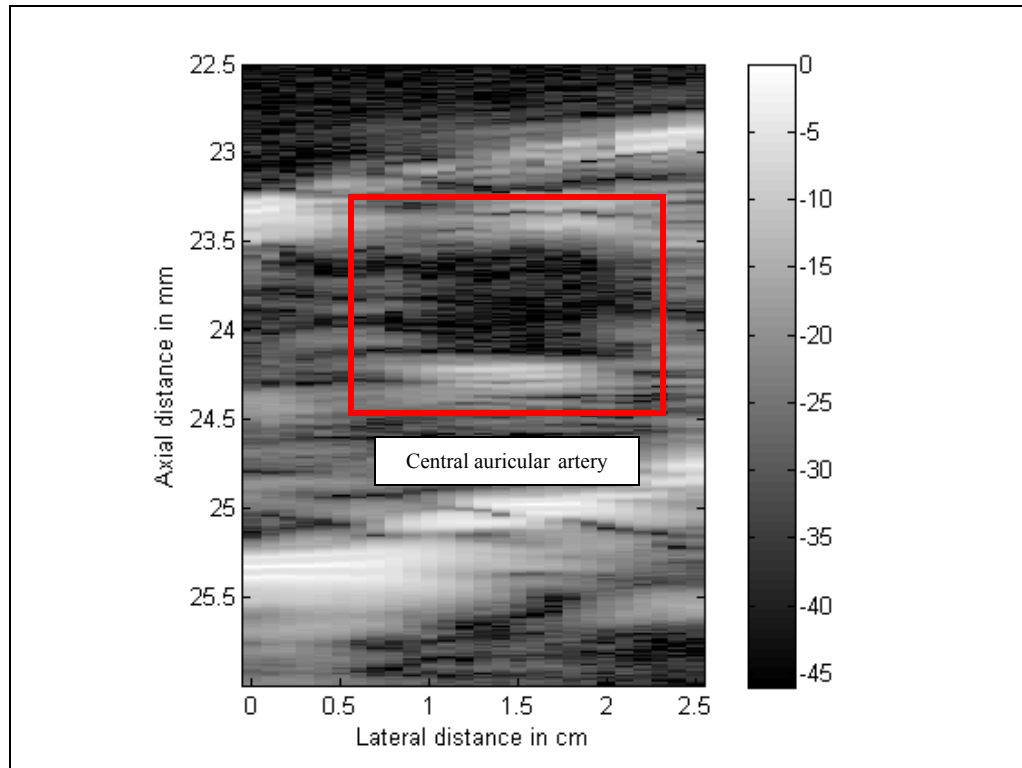


Figure 3.5 Setup of in vivo experiments.



**Figure 3.6 B-mode image of central auricular artery in absence of UCAs.**

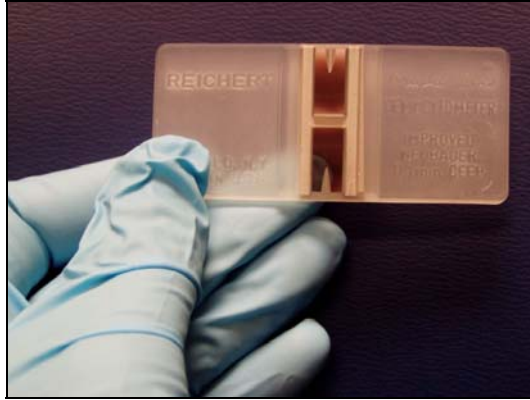


Figure 3.7 Image of a hemacytometer.

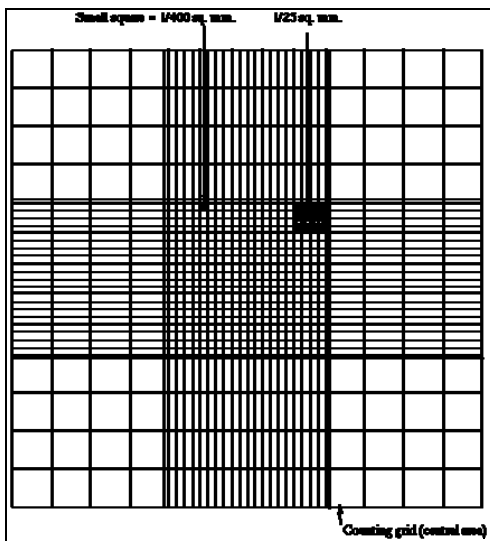


Figure 3.8 Hemacytometer grid.

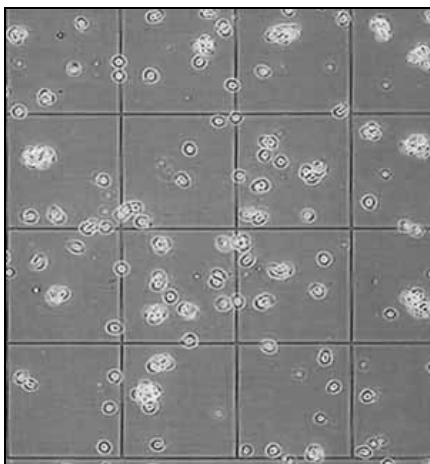
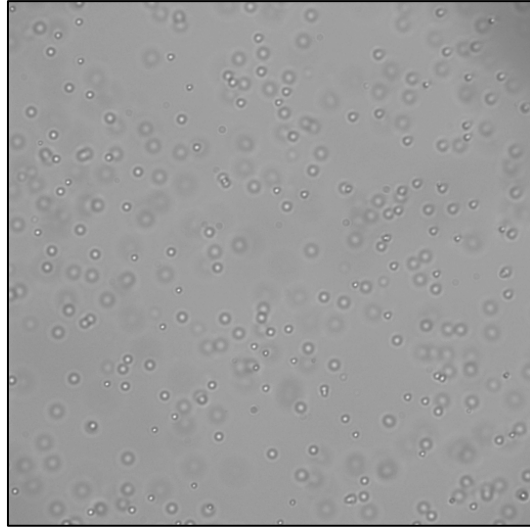
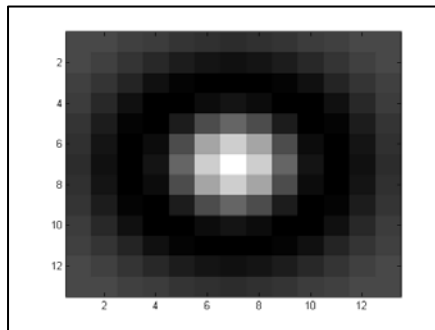


Figure 3.9 Image of microbubbles on top of hemacytometer grid.



**Figure 3.10** Image of latex spheres.



**Figure 3.11** Example of 2-D mask used to convolve over image file.

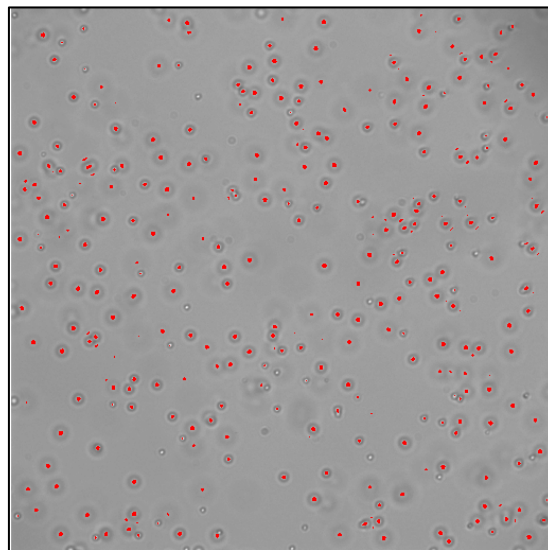


**Figure 3.12** Circle detection results (red circles) superimposed onto image file.

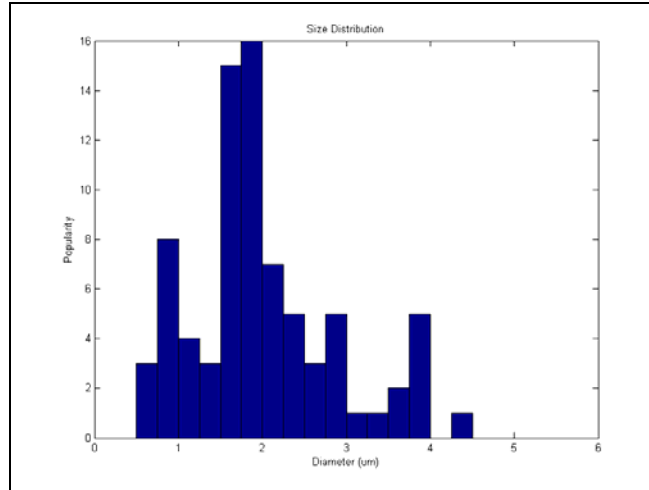


Figure 3.13 Size distribution of UCAs obtained using spatial domain analysis technique.

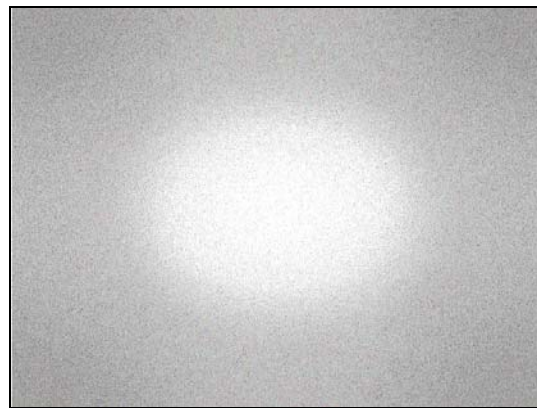


Figure 3.14 2-D Fourier transform of input image file.

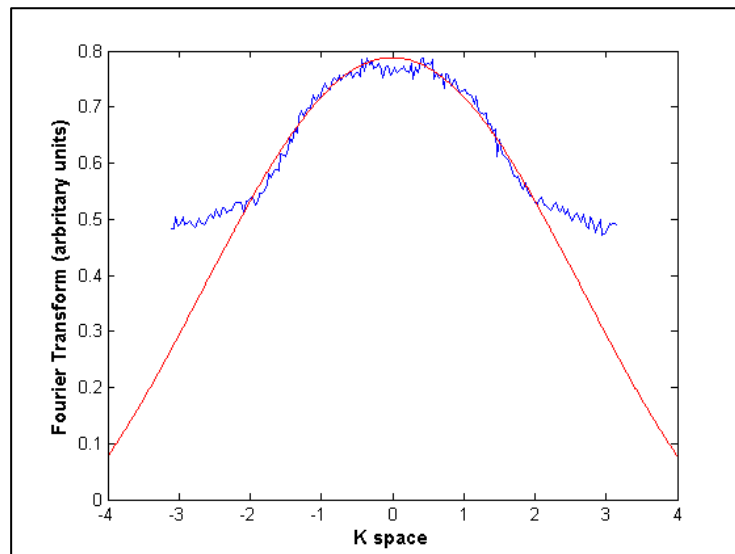
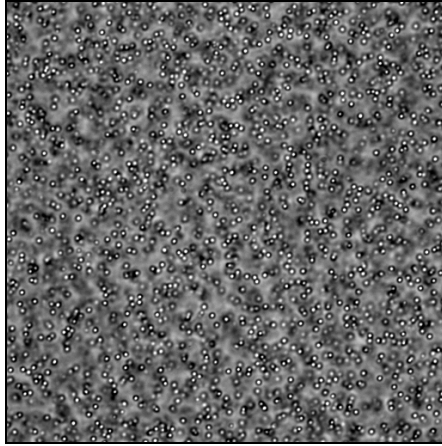
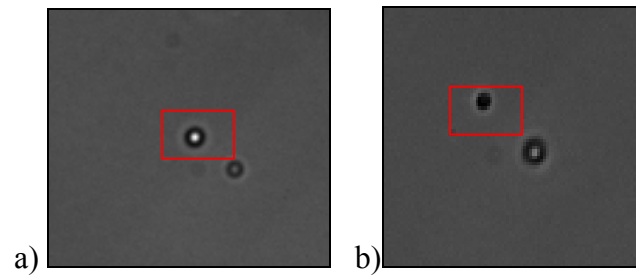


Figure 3.15 Fitting a jinc function (red line) to a 1-D horizontal slice (blue line) of the 2-D Fourier transform of the input image file.



**Figure 3.16** Image of latex spheres under a fluorescence microscope.



**Figure 3.17** Latex sphere (a) in focus and (b) out of focus. In (b), the spatial analysis program was unable to detect and analyze the sphere due to the absence of a white nucleus.

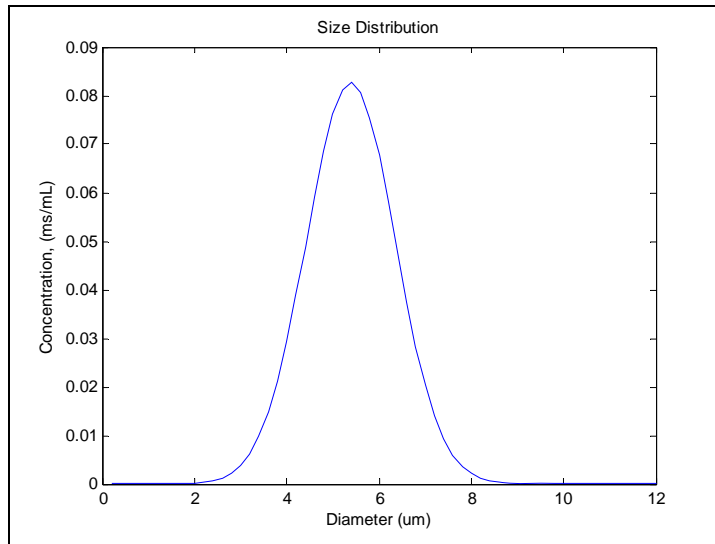


**Figure 3.18 Gaussian distribution of microbubble sizes (concentration is given in  $10^6$  ms/mL).**

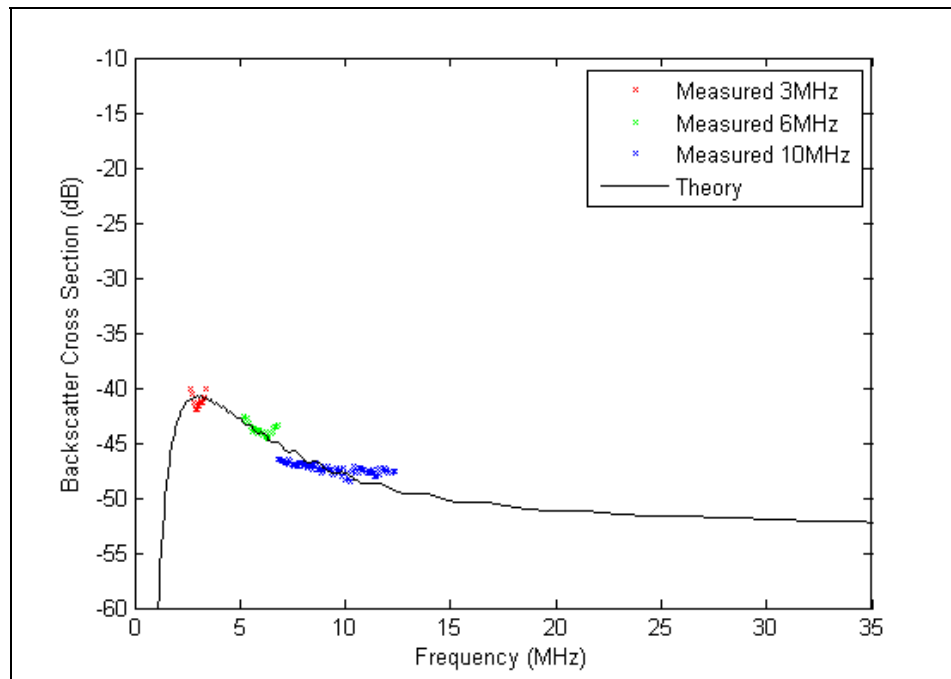


**Figure 3.19 Comparing theoretical and measured backscatter cross section.**

### 3.8 Tables

**Table 3.1 Properties of transducers.**

Center Frequency	3-MHz	6-MHz	10-MHz	20-MHz
Model Number	04196	04199	02288	07573
-6-dB Bandwidth	0.671 MHz	1.648 MHz	5.55 MHz	5.62 MHz
F-Number	3	3	4	3
Aperture Diameter	19 mm	19 mm	12.7mm	6.4 mm
Focal Length	57 mm	57 mm	50.8 mm	19.2 mm
Manufacturer	Valpey Fisher	Valpey Fisher	Valpey Fisher	Valpey Fisher

**Table 3.2 Rarefactional pressure at focus of transducer in beaker experiments (MPa). Values in bold represent the largest values used that were below the estimated threshold of collapse.**

Transducer Frequency	Energy ( $\mu$ J)			
	12.5	25	50	100
3-MHz	<b>0.585</b>	0.929	1.268	1.514
6-MHz	<b>0.883</b>	1.324	1.678	1.866
20-MHz	1.391	1.847	<b>1.986</b>	1.956

Transducer Frequency	Energy ( $\mu$ J)			
	4	8	16	32
10-MHz	0.25186	0.43023	0.60202	<b>0.7245</b>

**Table 3.3 Rarefactional pressure at focus of transducer in perfusion phantom experiments (MPa). Values in bold represent the largest values used that were below the estimated threshold of collapse.**

Transducer Frequency	Energy ( $\mu$ J)			
	12.5	25	50	100
3-MHz	0.00326	0.00584	0.00991	<b>0.0184</b>
6-MHz	0.00992	0.0157	0.0213	<b>0.0241</b>

**Table 3.4 Panametrics settings used for different transducers.**

Transducer Center Frequency (MHz)	3	6	10	20
Panametrics Model Number	5800	5800	5900	5800
Pulse Repetition Frequency (PRF) (kHz)	2.00	2.00	2.00	5.00
Input Energy ( $\mu$ J)	12.5	12.5	32	50
Damping ( $\Omega$ )	50	50	50	50

**Table 3.5 Diameter of latex spheres as determined by spatial and Fourier domain analysis.**

	<b>Latex Sphere Diameter (<math>\mu\text{m}</math>)</b>
<b>Spatial Domain Analysis</b>	1.025 $\pm$ 0.188
<b>Quoted</b>	1.025 $\pm$ 0.01

**Table 3.6 Latex sphere diameter measurements when sphere was in focus and out of focus.**

	<b>Diameter (<math>\mu\text{m}</math>)</b>				
<b>Different Foci</b>	<b>Sphere 1</b>	<b>Sphere 2</b>	<b>Sphere 3</b>	<b>Sphere 4</b>	<b>Sphere 5</b>
1	1.198	1.417	Did not detect	1.493	Did not detect
2	Did not detect	0.964	Did not detect	Did not detect	Did not detect
3	Did not detect	Did not detect	1.017	1.13	Did not detect
4	0.964	Did not detect	Did not detect	Did not detect	1.417
5	Did not detect	Did not detect	Did not detect	Did not detect	1.377
6	1.377	1.377	Did not detect	1.528	1.417
7	Did not detect	Did not detect	1.377	1.528	0.882
8	1.292	1.456	1.417	1.493	0.998
<b>Standard Dev.</b>	<b>0.178</b>	<b>0.228</b>	<b>0.220</b>	<b>0.171</b>	<b>0.258</b>

## CHAPTER 4: RESULTS

### 4.1 In Vitro Experiments

#### 4.1.1 Beaker experiments

Figure 4.1a-d are representative power spectra of the UCA backscatter within a beaker created by averaging the power spectra from 500 samples. The peaks in the power spectra around 3 MHz, 6 MHz, 10 MHz, and 20 MHz, i.e., the center frequencies of the respective insonifying transducers, are evidence of the presence of microbubbles.

As expected, a stronger initial backscattered power response was observed from higher concentrations of Definity than from lower concentrations. However, we also observed a consistent exponential decay in the magnitude of the backscattered power with time. This exponential decay was present independent of the active transducer's frequency as shown in Figure 4.2-4.6. Figure 4.2 also illuminates a significant difference between the initial backscattered power when the Definity was used immediately after Vialmix activation (see pink solid lines in Figure 4.2) and when it was used a few hours after Vialmix activation (see blue dashed lines in Figure 4.2) (Note: After Vialmix activation, the Definity was placed inside a refrigerator at 6°C). For the sake of conserving Definity, experiments with the 3 MHz, 10 MHz, and 20 MHz transducers were conducted on "After Vialmix" samples only.

The exponential decay in the peak power spectra amplitude versus time suggests either a decrease in concentration of Definity, a reduction in the average size of the microbubble population, or both. A decrease in the average microbubble size over time would also explain why the backscattered signal was larger when Definity was used immediately after Vialmix activation (pink lines in Figure 4.2) compared to when the samples were used a few hours after Vialmix activation (blue lines in Figure 4.2). Our first inclination was to attribute the decay in backscattered power to a decay in average microbubble size rather than concentration because backscattered power has a second-order dependence on the volume of the scatterer while having only a first-order dependence on concentration (see Equation (2.1)). Therefore, changes in the size of the scatterer will have a greater effect on the magnitude of the backscattered power than changes in concentration. Some possible causes for the decay in concentration or mean

bubble size include: (1) degassed water being an incompatible medium, which would cause the membrane shell of the microbubbles to dissolve and create free bubbles, or (2) the acoustic field causing microbubbles to collapse.

The decay in backscattered power was quantized using half-lives, which are documented in Table 4.1. Half-lives were estimated for different concentrations of microbubbles, for different ultrasonic frequencies of interrogation used and for “after Vialmix” versus “out of refrigerator.” The half-life was estimated by fitting an exponential function to the measured backscattered power decay. Then using the equation given for the best-fit exponential function, we solved for the time required to reach half the maximum value. T-tests were performed on the estimates of the half-lives tabulated in Table 4.1 and the results of the t-tests are displayed in Table 4.2-4.4. If  $|t| < 2$ , then there was no statistically significant difference between the two half-lives. If  $|t| > 3$ , then there was statistically significant difference between the two half-lives, and if  $2 < |t| < 3$ , then more samples are required to make a conclusive evaluation.

From the experiments, all t values were found to be less than 2, indicating that the half-life of Definity microbubbles is independent of frequency and concentration. No statistically significant differences were observed in the half-lives of the samples examined immediately after the Vialmix activation and samples out of the refrigerator. All half-lives were within the range of 5-8 min.

To test if the exponential decay in backscattered power was due to a compatibility issue between Definity microbubbles and degassed water, experiments were conducted with the Definity microbubbles immersed in isotonic 0.9% saline solution. Figure 4.6 shows plots of the exponential decay curves of the Definity microbubbles immersed in isotonic 0.9% saline solution. Half-lives and t-test results for the 0.9% saline solution are tabulated in Table 4.5 and Table 4.6. Because in all cases,  $|t|$  was less than two, the results in Table 4.6 indicate that there are no statistically significant difference between the half-lives of samples where degassed water was the medium versus a medium of 0.9% saline solution. This suggests that the decay in backscattered power is unrelated to the medium.

Another hypothesized cause for the gradual decay in contrast agents over time was the destruction of microbubbles from the acoustic pressure induced by the transducer. Although experiments used pressure values less than the acoustic rarefactional pressure

required to initiate inertial cavitation, previous studies have suggested that even at low pressures, the acoustic pressure can cause lesions in the shells of the microbubbles. This enables the enclosed gas to escape into the medium and create free bubbles [22]. To test this hypothesis, the transducer was switched off between snapshots instead of continuously exposing the sample to an acoustic field. In theory, if the acoustic field was the cause of the UCA collapse, we would observe a significant increase in the half-life of the Definity microbubbles when the transducer was turned off between snapshots. Experiments were only performed on 0.1x concentration samples.

Figure 4.7 shows plots of the exponential decay curves of the Definity microbubbles when the transducer was switched off between acquiring snapshots. Half lives and t-test results for this condition are tabulated in Table 4.7 and Table 4.8. T-test results listed in Table 4.8 indicate no statistically significant differences in the half-lives for the 0.1x concentration samples when the transducer remained on compared to samples when the transducer was switched off between snapshots (see Table 4.7). In either case, the half-lives were around 5 to 6 min, indicating that the acoustic pressure generated by the transducer had little to no effect on the time-dependent decay of the backscattered power. The accumulation of these results suggests that the decay of backscattered power with time is characteristic of the Definity microbubbles independent of externalities. Therefore, estimates of the concentration of the UCA need to factor in the decay of microbubble scattering with time. This phenomenon can be accounted for by using the Monte Carlo technique to fit for size distribution and concentration at one time.

#### **4.1.2 Perfusion phantom experiments**

Figure 4.8a, b are representative of the raw power spectrum (i.e., not normalized nor attenuation corrected) obtained from averaging the power spectra of 150 snapshots of the UCA mixture within the perfusion phantom. The peaks in the power spectrum at around 6 MHz (see Figure 4.8a) and 3 MHz (see Figure 4.8b), i.e., the respective center frequencies of the insonifying transducers, indicate the presence of microbubbles within the window of observation.

Differences in the backscatter power estimates were observed between the three concentrations of Definity, 0.1x, 1x and 2x, even through 1/16 inch of silicon tubing as

the UCAs were in motion. Table 4.9 tabulates the values of the average normalized backscattered power for the different UCA concentrations measured within the perfusion phantom. Note that the predicted level of the backscattered power should increase proportionally to the number density, i.e, a 2x change in the number density should lead to a 2x change in the backscattered power. While the estimated backscattered power increased with increasing number density, the increase was not by the same factor as the predicted increase in number density.

## 4.2 Concentration of UCA Population

As mentioned in Chapter 2.2, the backscatter cross section is linearly proportional to the concentration of scatterers. And because the backscatter cross section, like backscattered power, is a second-order function, we expect a two-fold increase in concentration to produce a two-fold increase in the initial backscattered power. Table 4.10 lists the ratios of the initial backscattered power for various concentrations of Definity when measured within a beaker of degassed water using the 3 MHz, 6 MHz, 10 MHz and 20 MHz transducers. Table 4.11 tabulates the ratios of the initial backscattered power for various concentrations of Definity samples when measured within the perfusion phantom using a 3 MHz and 6 MHz transducer.

The ratios in Table 4.10 and Table 4.11 did not reflect the predicted increase in backscattered power, which was a linear relationship between the concentration ratios and the ratio of the initial backscattered power. However, when the concentration of microbubbles was measured using a hemacytometer (see Table 4.12), it was discovered that the concentration ratios measured by the hemacytometer were close to the ratios predicted by the ultrasound backscattered power (see Table 4.13). The inconsistencies in Table 4.10 and Table 4.11 were then attributed to the preparation technique. The concentrations referred to as 0.1x, 1x, and 2x with respect to the clinical standard dosage did not accurately reflect the relative ratios.

Using the hemacytometer, we were able to estimate the concentration of microbubbles in the 0.1x, 1x, and 2x samples. On average, the 0.1x concentration contained  $5.722 \times 10^5$  microspheres/mL, the 1x concentration contained  $1.737 \times 10^6$  microspheres/mL, and the 2x concentration contained  $2.759 \times 10^6$  microspheres/mL. The

ratio estimated using the hemacytometer of the 0.1x:1x concentrations was 3.306, the ratio of the 1x:2x concentrations was 1.589, and the ratio of the 0.1x:2x concentrations was 4.823. Therefore, the ratios estimated by the ultrasonic technique closely matched the ratios estimated through the hemacytometer, suggesting that the ultrasonic technique was successful at estimating relative concentrations.

### **4.3 Size Distribution of UCA Population**

The initial motivation for characterizing the size distribution of Definity microbubbles was to explain the difference in backscattered power between samples observed immediately after Vialmix activation and those observed a few hours after Vialmix activation. We hypothesized that a population of larger microbubbles was the reason for the more intense backscatter from samples observed immediately after Vialmix activation, but expected to see a relatively narrow distribution of bubble sizes.

As mentioned, a decrease in the mean bubble size would explain the difference in initial backscattered power between the samples observed immediately after Vialmix® activation and those observed a few hours after activation. The left column of Figure 4.9 displays sample images of Definity microbubbles immediately after Vialmix activation. Their corresponding size distribution histograms are in the right column. The same holds for Figure 4.10, except the images are of microbubbles 30 min after Vialmix activation. The histograms indicate that the dominant populations of microbubbles in samples observed immediately after Vialmix activation are centered around 2 to 3  $\mu\text{m}$  in diameter. In contrast, the samples observed 30 min after activation have dominant populations around 1  $\mu\text{m}$  in diameter.

Figure 4.11 and Table 4.14 indicate that the average diameter of the microspheres decreased from 2.636  $\mu\text{m}$  to 1.439  $\mu\text{m}$  within the 30 min span after Vialmix activation. The variation in bubble sizes was also greater in the samples immediately after Vialmix activation compared to those 30 min after Vialmix activation.

Size distributions of the microbubble population over a 35 min time period in intervals of 5 min were also optically observed. Visual confirmation that the average bubble size was decreasing with time confirmed that the decay in backscattered power over time was due to an overall decrease in average bubble size (refer to Figure 4.2

and Table 4.15). Images also indicated a decrease in concentration over time. However, because the backscattered power is proportional to the volume of the scatterer squared and only linearly proportional to the concentration of scatterers, the decrease in average bubble diameter typically has a much greater effect on the reduction of backscattered power. This decay in the average size further illustrates the need to use multiple parameters to acquire fits of the measured power spectra to theoretical power spectra in order to obtain a realistic estimate of the instantaneous UCA concentration.

#### **4.4 In Vivo Experiments**

##### **4.4.1 In vitro backscatter power measurements in blood medium**

In the bloodstream, both blood cells and UCAs will contribute to the backscattered signal. In order to quantify the effects of blood on the backscatter, in vitro experiments of the same nature as those described in Section 3.2 were conducted. However, instead of degassed water being the medium, we conducted the quantitative analysis of UCAs within a blood medium with differing hematocrit values. The goal of these experiments was to gain insight into the response of UCAs to an acoustic field in vivo and to determine the relative contribution of UCAs and blood to ultrasound backscatter. An understanding of this contribution would enable the estimation of UCA concentration in the bloodstream by comparison of ultrasonic backscatter to appropriate models. The UCA backscattered power as a function of time is shown in Figure 4.12.

As before, we observed an exponential decrease in backscattered power over time. However, we also observed a noticeable decrease in the UCA backscattered power as hematocrit value increased. Possible explanations for this phenomenon include the following: (1) larger hematocrit values result in increased attenuation of the pulse-echo acoustic signal and/or (2) the change in hematocrit values results in a change in the background impedance and consequently the impedance mismatch between background and UCA. Simulation results that do not account for attenuation through blood (shown in Figure 4.13) as well as literature values ([25] and [26]), predict this slight decrease in UCA backscatter power with increasing hematocrit value. Extrapolating theoretical backscatter power for the 40% hematocrit case at 10 MHz (shown in Figure 4.13) and multiplying this value by the measured UCA 1x concentration of  $1.737 \times 10^6$

microspheres/mL, indicates that the UCA backscatter power should be  $\sim 2.5$  dB above the power scattered by blood only for the 1x concentration case. Therefore, this indicates we should be able to distinguish backscatter due to blood from the backscatter due to UCAs. To estimate the absolute concentration of UCAs in vivo, it is necessary to account for the contribution of backscatter from blood.

#### **4.4.2 In vivo experiments within central auricular artery**

The ultrasonic technique was then used to estimate the change in UCA concentration in the auricular artery of a rabbit injected with various concentrations of Definity. Figure 4.14a, b are B-mode images of the central auricular artery. Darker shades of gray represent weak scattering and lighter shades of gray represent strong backscatter. Because blood is a weak scatterer of ultrasound over the frequency range of 3 to 20 MHz, the artery is easily identified as the circular anechoic dark region. These images confirm the dimensions of the artery, which is approximately 1 mm in diameter. The increased speckle within the auricular artery in Figure 4.14b illustrates our ability to detect the presence of microbubbles in vivo.

In vivo experiments proved challenging due to the size of the central auricular artery. Depending on the age and weight of the rabbit, sometimes the artery would be clearly visible as observed in Figure 4.14. On other occasions, the artery was narrow and barely resolvable. In the latter case, backscatter from the cloud of bubbles was barely observable on the RF lines. Fortunately, the few times where the artery was wide enough, we did observe a difference in the backscatter from varying concentrations of Definity. Moreover, the proportions of backscattered power corroborated theory (i.e., a two-fold increase in UCA concentration resulted in a doubling of the backscattered power), as seen in Table 4.16. In Figure 4.15, the backscattered power is monitored over time. For all concentrations, we observed an initial spike in the backscattered power as the initial cloud of contrast agents passed through the focus of the transducer. Following the initial peak, the backscattered power then returned to baseline. The difference between the peak power values and baseline were used to approximate the ratio of microbubble concentrations.

The results from Table 4.16 show good correlation between the expected and measured backscattered power ratios for all concentrations. These preliminary results suggest that an effect can be measured and the relative concentration of UCAs can be estimated in vivo over time if a large vessel can be resolved using appropriate frequencies. To estimate the actual concentration of UCAs at any instant of time, the measured ultrasonic backscatter power spectrum must be fit to a theoretical backscattered power spectrum that incorporates the scattering from blood, average radius, and variance of the UCA radius.

#### **4.5 Theory vs. Measured Backscatter Cross Section**

Results from the sizing of UCAs were used to construct the theoretical UCA backscatter cross section model (refer to Figure 4.16). Using the 3 MHz and 6 MHz in vitro beaker data, a maximum of -7 dB was observed between the measured and theoretical UCA backscatter cross section (refer to Figure 4.17, Figure 4.18, and Figure 4.19). This comparison was performed to substantiate the theoretical backscatter model.

The objective of the Monte Carlo fitting routine was to determine the parameters of mean UCA size and standard deviation of sizes that resulted in a best fit of the theory to the measured data as quantified by the MSE. From these simulations, estimates of the mean bubble radius, variance, and concentration were obtained and compared against the mean and UCA concentration values obtained using the hemacytometer and image processing techniques.

Preliminary simulations involved fitting the theoretical model to individual measured data sets using the 3 MHz, 6 MHz and 10 MHz transducers (see Figure 4.20). However, because of the broadband frequency dependence of UCAs, these simulations did not produce results that supported experimental data. More rigorous simulations were later conducted by trying to fit the theoretical model to the 3 MHz, 6 MHz, and 10 MHz data sets simultaneously (see Figure 4.21). All Monte Carlo simulations were only performed on in vitro beaker measurements.

Results in Table 4.17 and Figure 4.22 show good correlation between the mean bubble size and concentration estimates obtained from Monte Carlo simulation versus hemacytometer/image processing analyses. The variance in microbubble sizes is

considerably different, but this may be the result of image processing inaccuracies. Nevertheless, these results are significant in showing the ability of the Monte Carlo fitting routine to estimate mean bubble radius and concentration in vitro. Success in the in vitro setting suggests that the Monte Carlo fitting routine would also be a viable option to quantify UCAs in the in vivo setting. However, more efficient methods of curve fitting may be useful in the rapid estimation of the UCA concentration and could be a subject of future work.

## 4.6 Figures

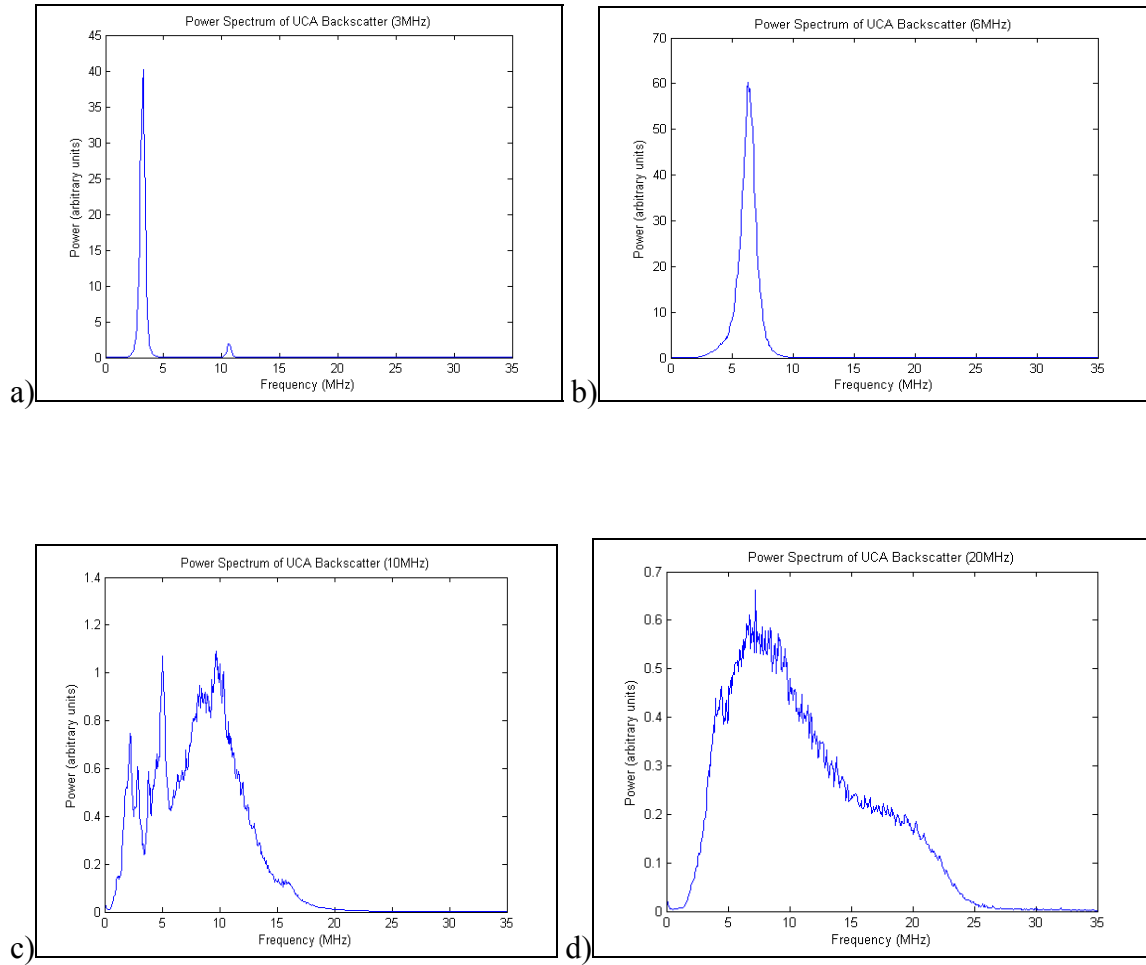
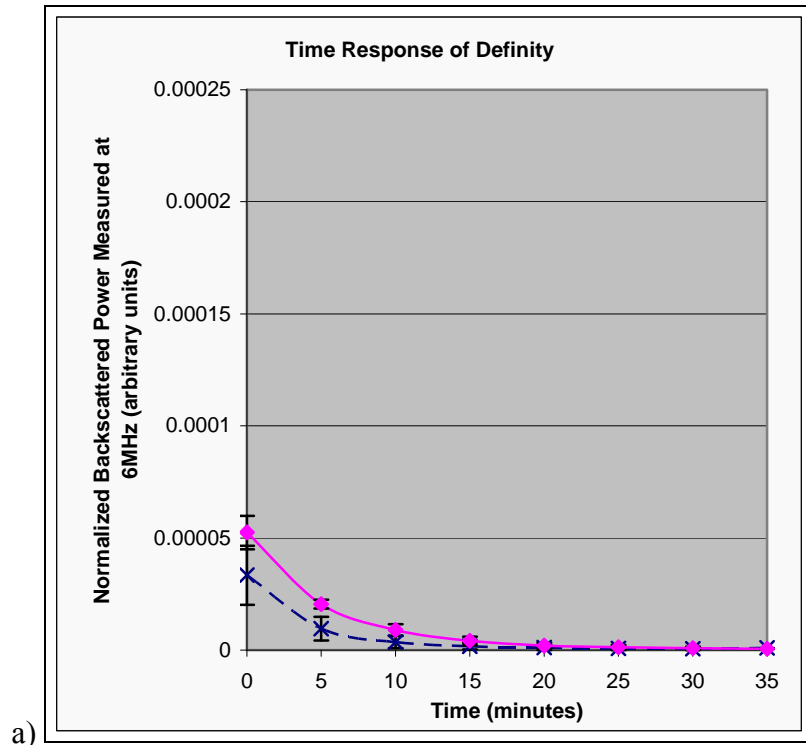
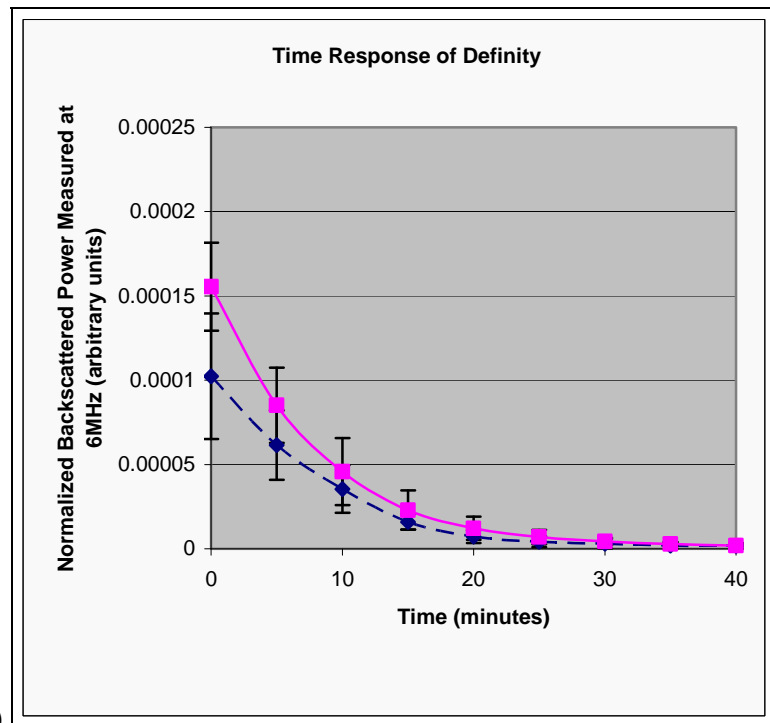


**Figure 4.1 Raw backscattered power spectra from UCAs using (a) 3 MHz, (b) 6 MHz (c) 10 MHz and a (d) 20 MHz transducer.**

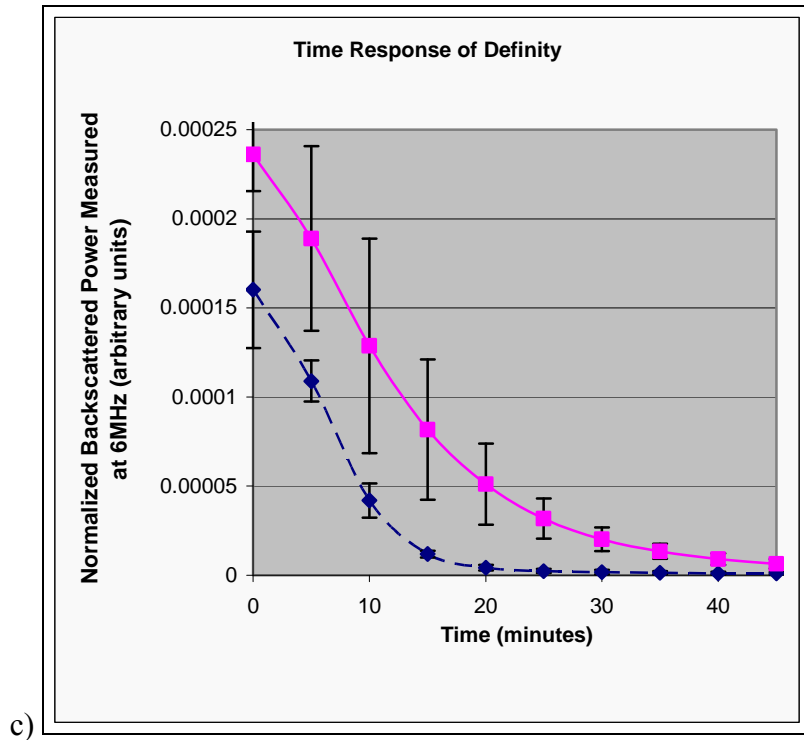


a)



b)

**Figure 4.2 Exponential decay of backscattered power with time for (a) 0.1x, (b) 1x, and (c) 2x concentrations of Definity in degassed water when insonified with a 6 MHz transducer. The pink solid lines indicate samples that were observed immediately after Vialmix activation and the blue dashed lines indicate samples observed after being in a refrigerator for a few hours after Vialmix activation.**



c)

Figure 4.2 continued.

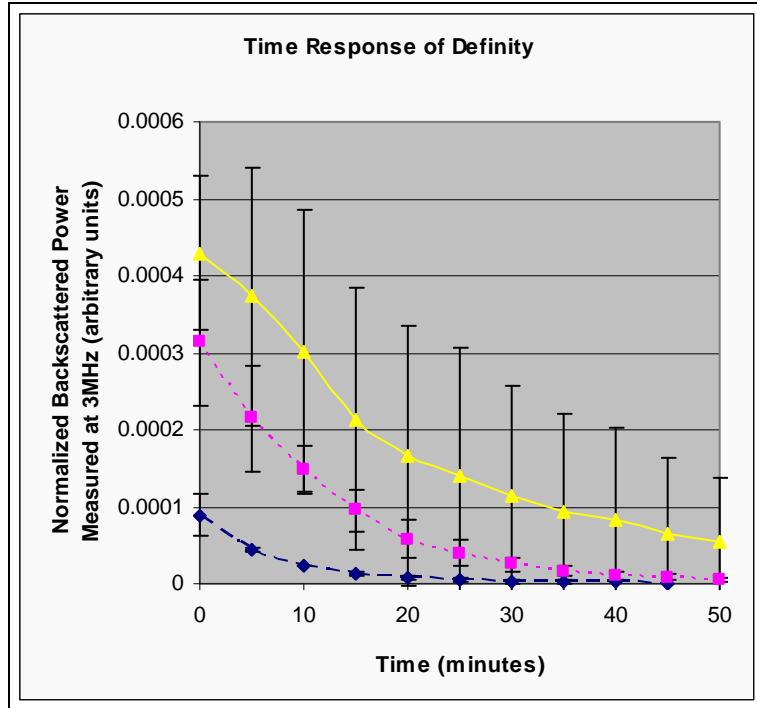


Figure 4.3 Exponential decay of backscattered power with time for 0.1x (blue dashed line), 1x (pink dotted line), and 2x (yellow solid line) concentrations of Definity in degassed water when insonified with a 3 MHz transducer.

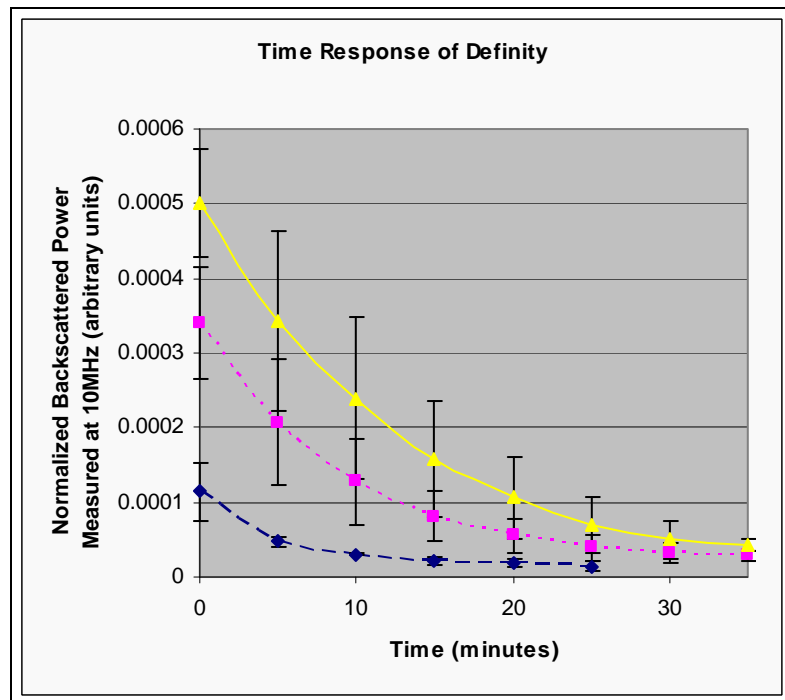
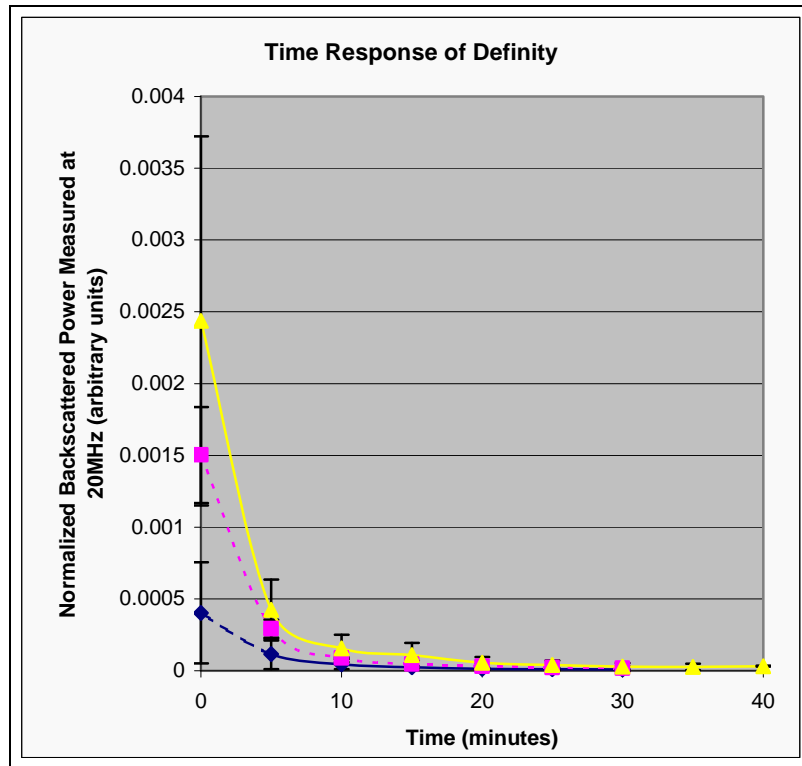
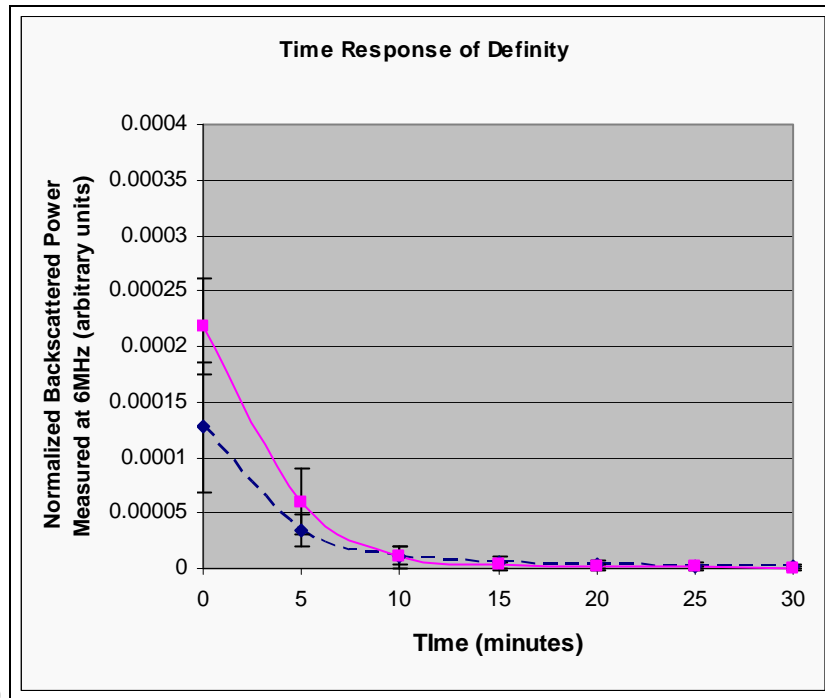


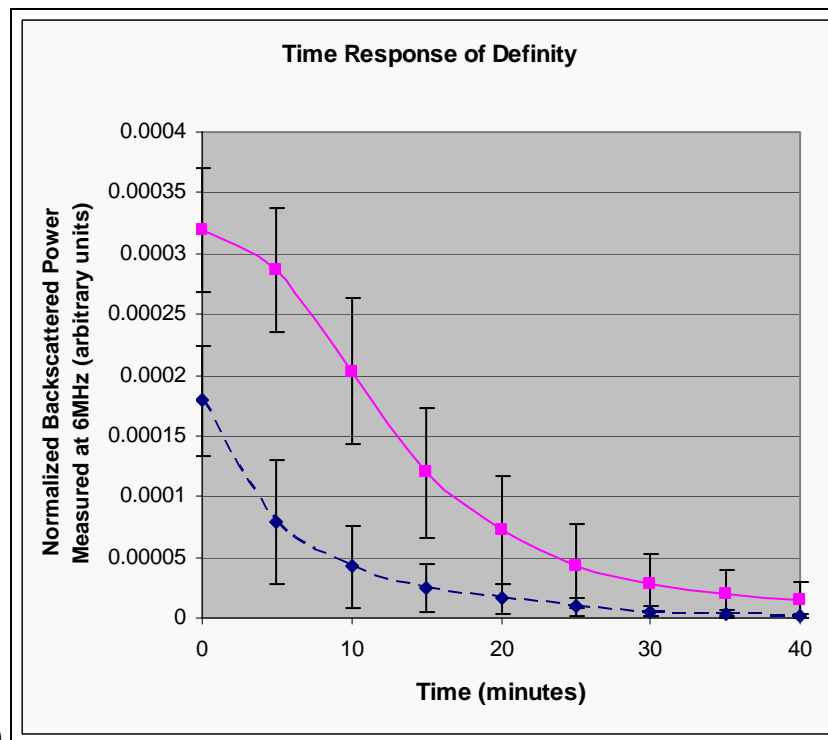
Figure 4.4 Exponential decay of backscattered power with time for 0.1x (blue dashed line), 1x (pink dotted line), and 2x (yellow solid line) concentrations of Definity in degassed water when insonified with a 10 MHz transducer.



**Figure 4.5 Exponential decay of backscattered power with time for 0.1x (blue dashed line), 1x (pink dotted line), and 2x (yellow solid line) concentrations of Definity in degassed water when insonified with a 20 MHz transducer.**



a)



b)

**Figure 4.6 Exponential decay of the backscattered power with time for (a) 1x and (b) 2x concentrations of Definity in 0.9% saline solution when insonified with a 6 MHz transducer. The pink solid lines indicate samples that were observed immediately after Vialmix activation and the blue dashed lines indicate samples observed after being in a refrigerator for a few hours after Vialmix activation.**

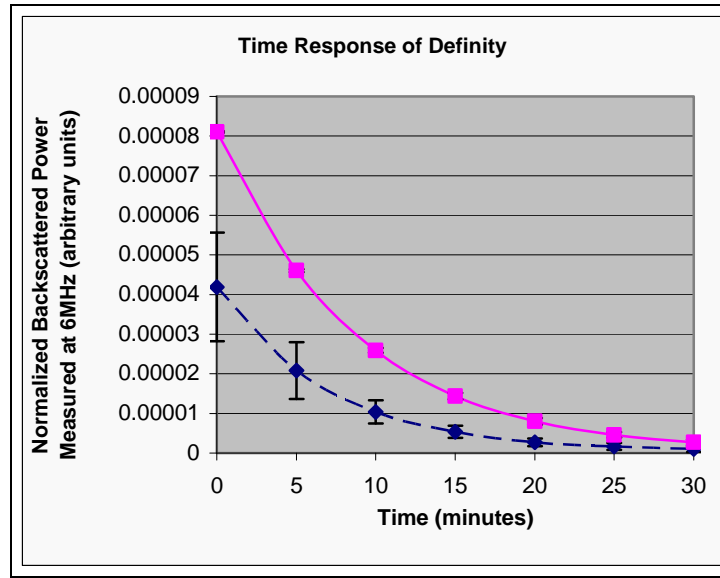


**Figure 4.7** Exponential decay of backscattered signal with time in 0.1x concentration of Definity with transducer switched off between snapshots. The pink solid line indicates samples that were observed immediately after Vialmix activation, and the blue dashed line indicates samples observed after being in a refrigerator for a few hours after Vialmix activation.

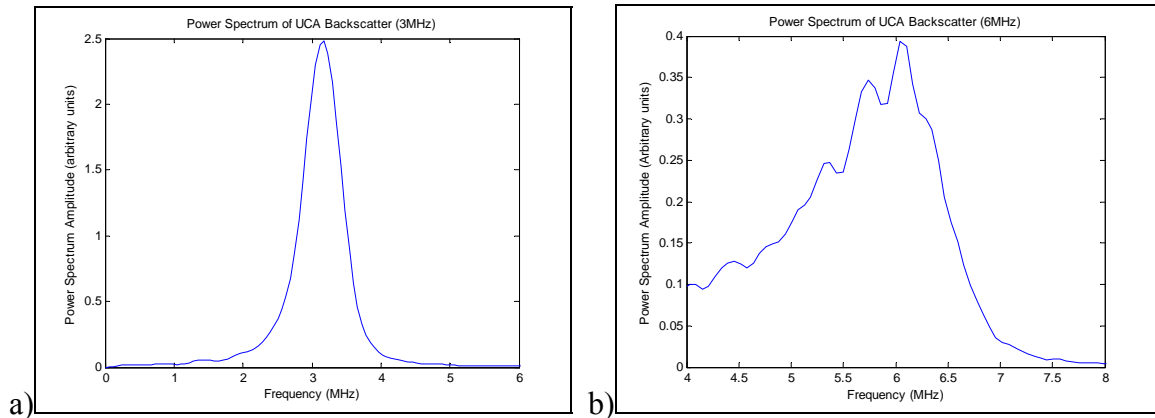


**Figure 4.8** UCA backscatter power spectra within perfusion phantom using (a) 3 MHz and (b) 6 MHz transducer.

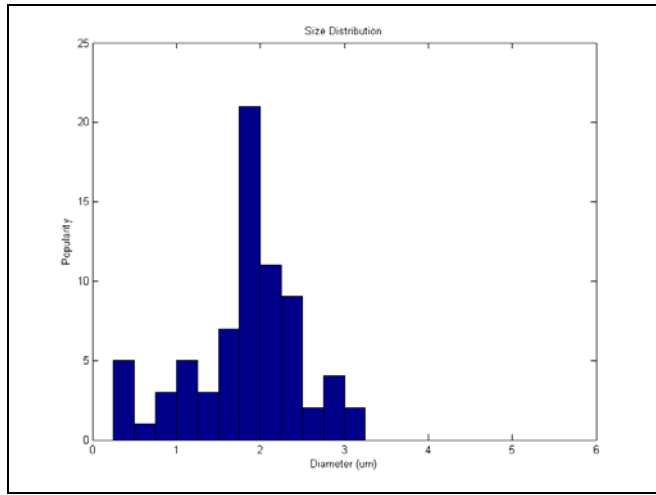
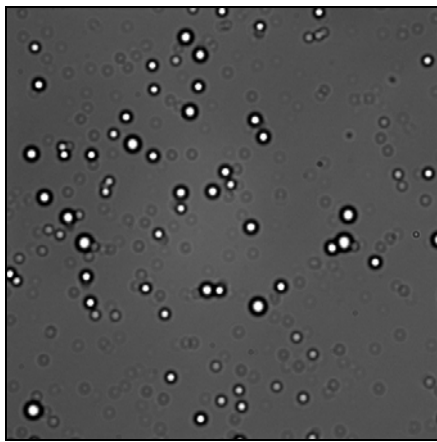
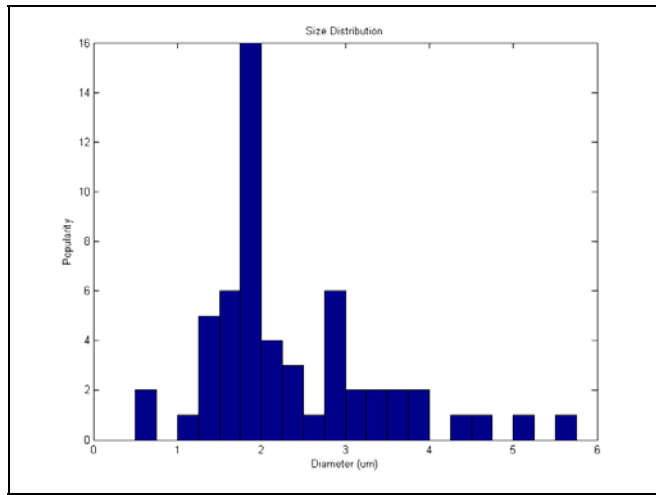
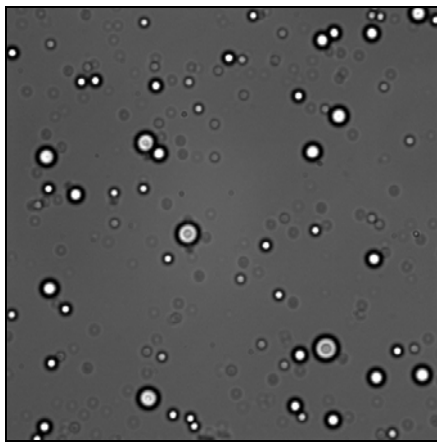
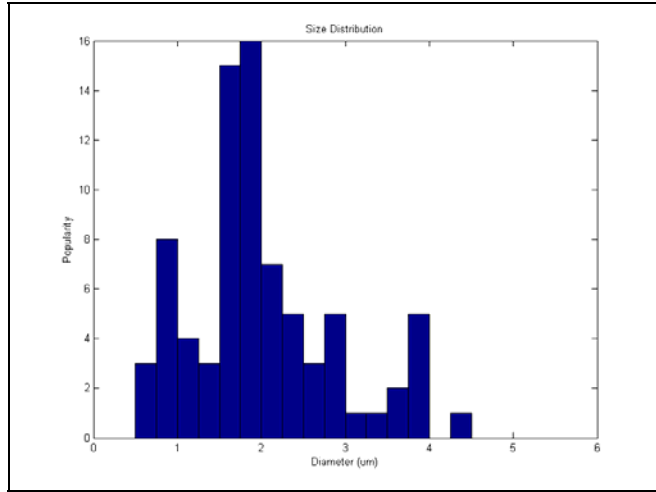
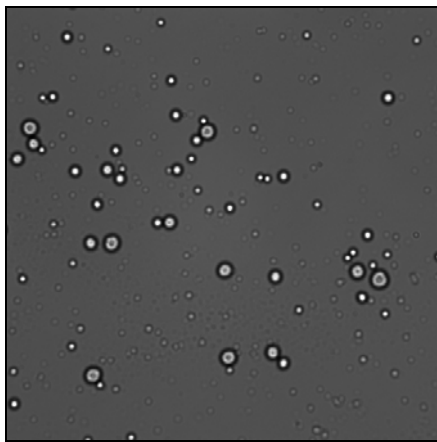


**Figure 4.9 Images (left column) and their respective size distributions (right column) of Definity microbubbles immediately after Vialmix activation.**

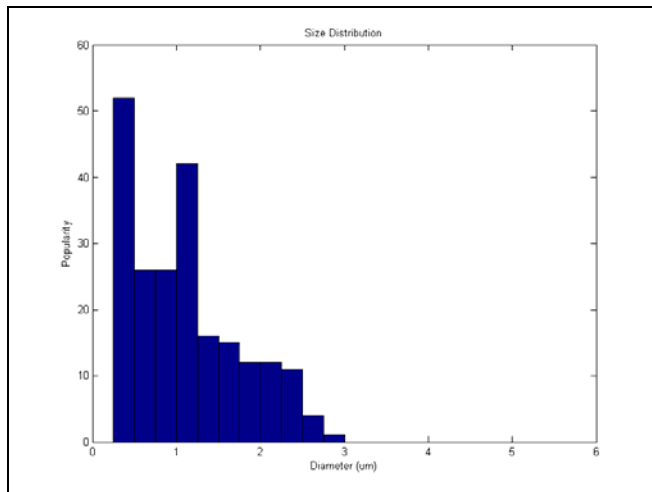
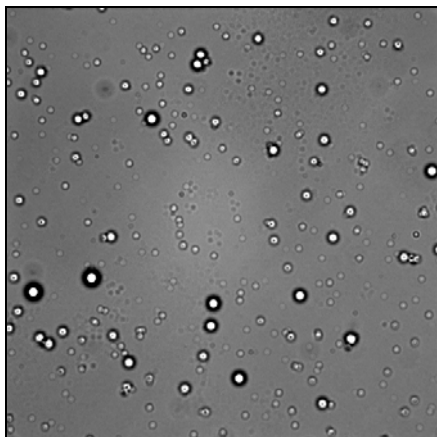
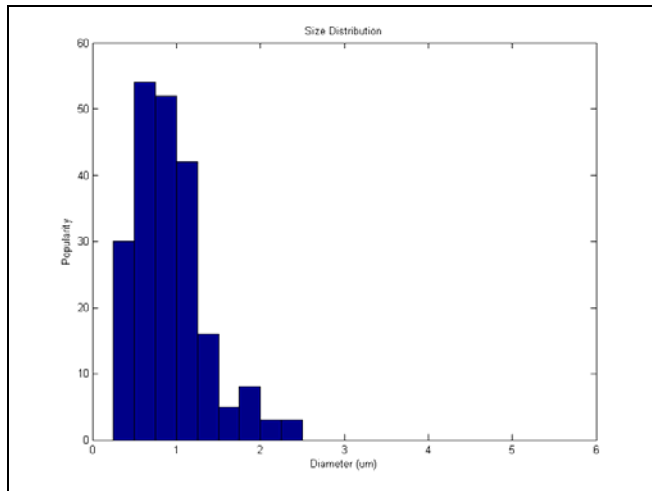
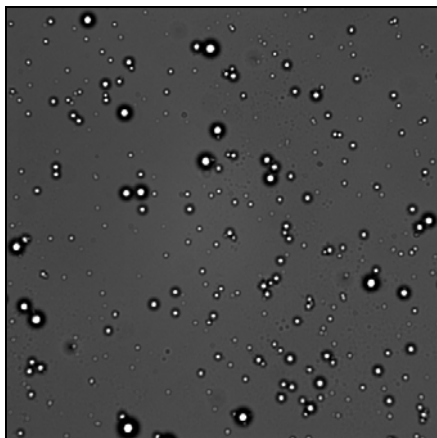
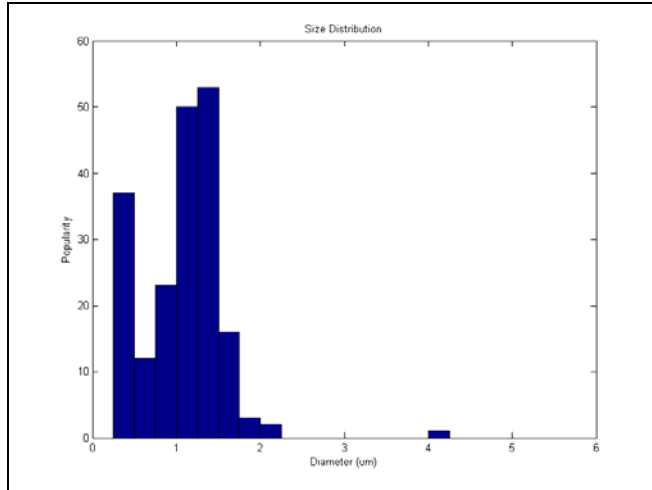
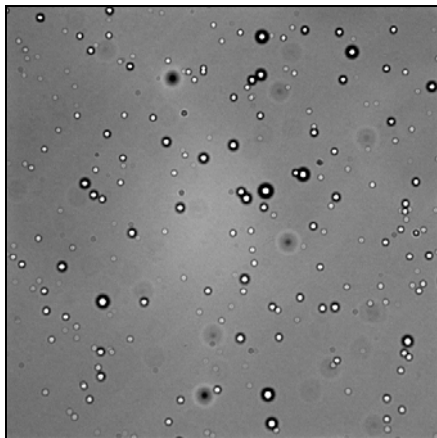


**Figure 4.10 Images (left column) and their respective size distributions (right column) of Definity microbubbles 30 min after Vialmix activation.**

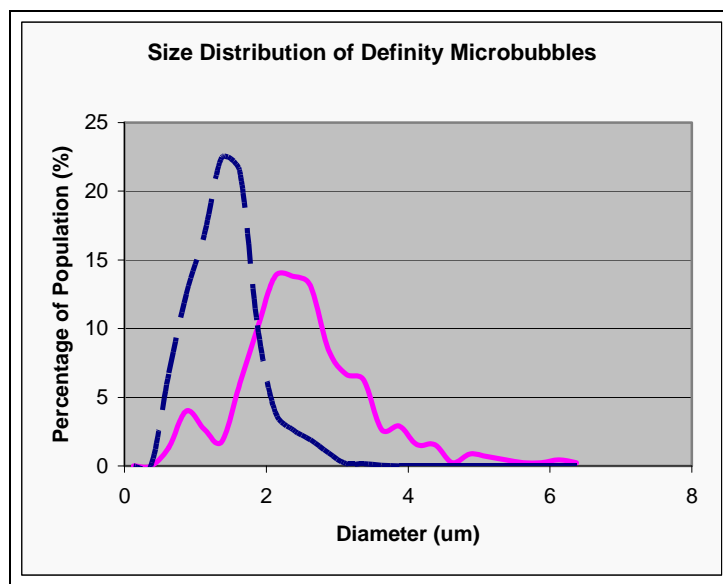


**Figure 4.11** Size distribution of Definity microbubbles. The pink solid line indicates samples that were observed immediately after Vialmix activation and the blue dashed line indicates samples observed 30 min after Vialmix activation.

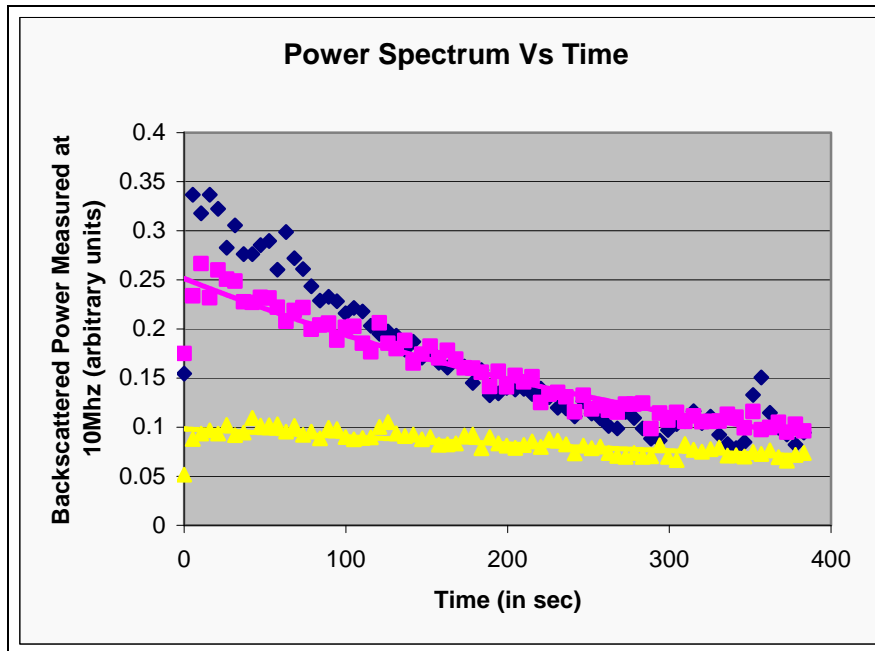


Figure 4.12 Backscattered power vs. time of UCAs in blood with varying hematocrit values. The yellow triangles represent 20% hematocrit values, the pink squares represent 10% hematocrit values and the blue diamonds represent 5% hematocrit values.

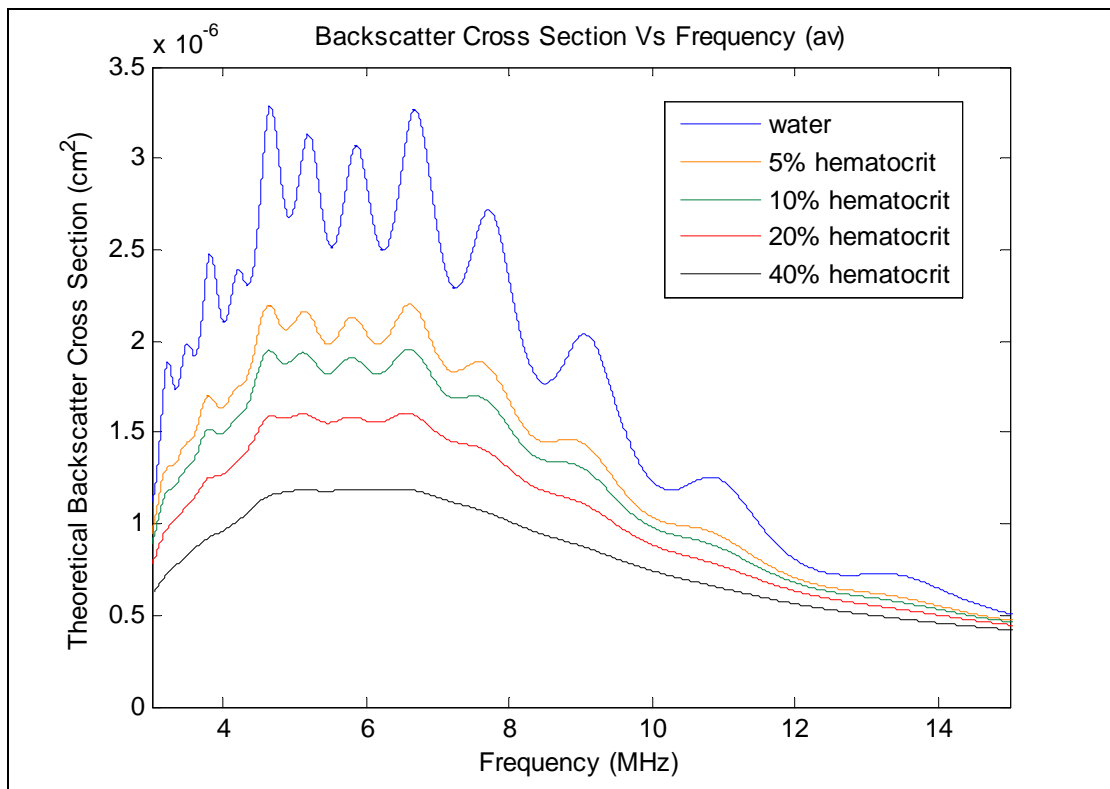
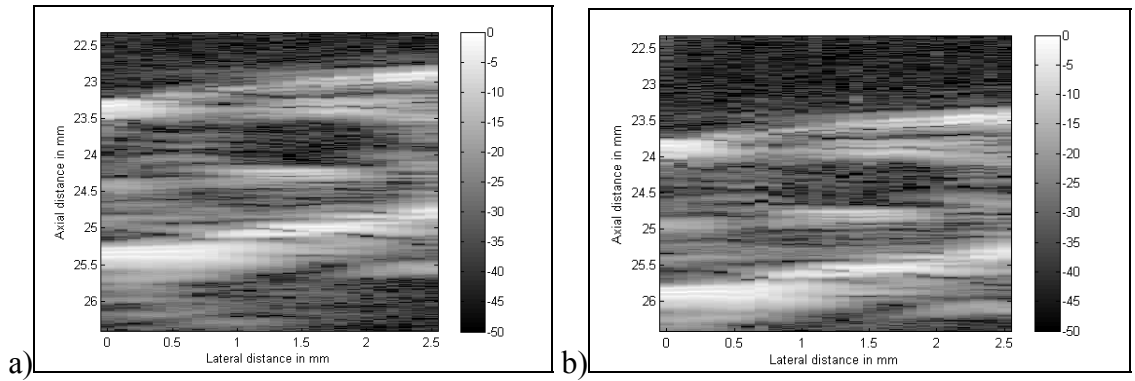
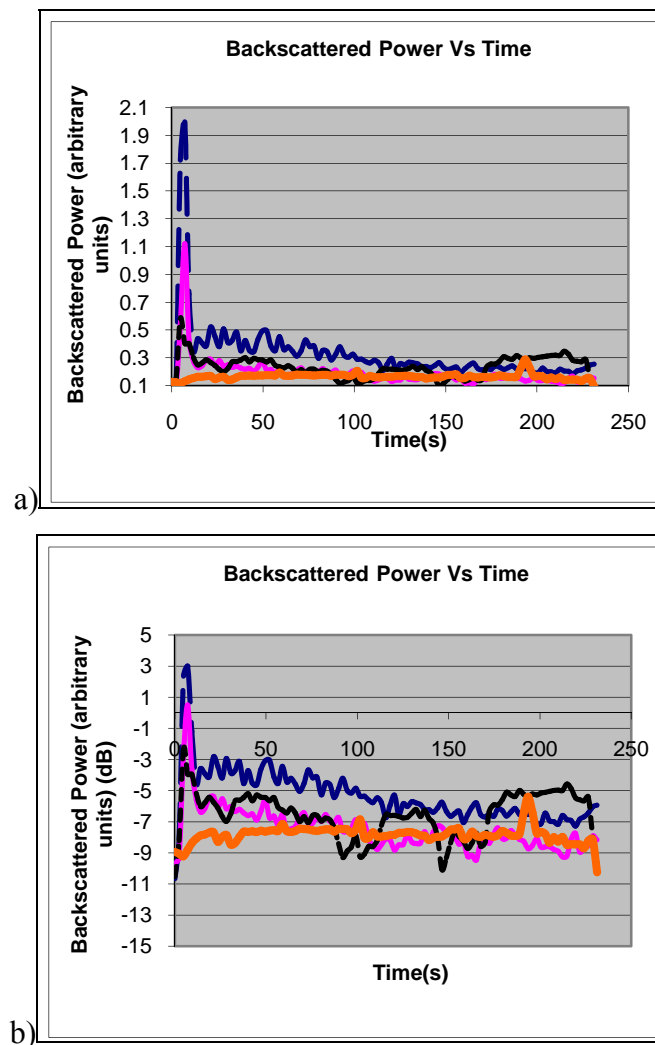


Figure 4.13 Theoretical UCA backscatter cross section vs. frequency in blood medium of varying hematocrit value and degassed water.



**Figure 4.14** Cross section B-mode image of central auricular artery (a) without Definity microbubbles and (b) with 5x concentration Definity microbubbles.



**Figure 4.15** In vivo backscattered power vs. time from different concentrations of Definity within the central auricular artery of a New Zealand white rabbit (a) linearly scaled and (b) logarithmically scaled. The dashed blue lines represent the 5x concentration, the solid pink lines are the 2x concentration, the black dotted lines are the 1x concentration, and the orange solid lines represent the baseline.

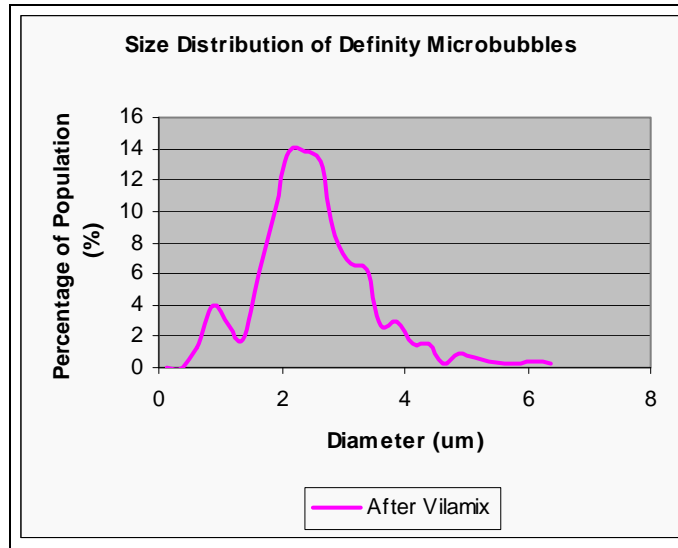


Figure 4.16 Size distribution of UCA used to construct theoretical backscatter cross section model.

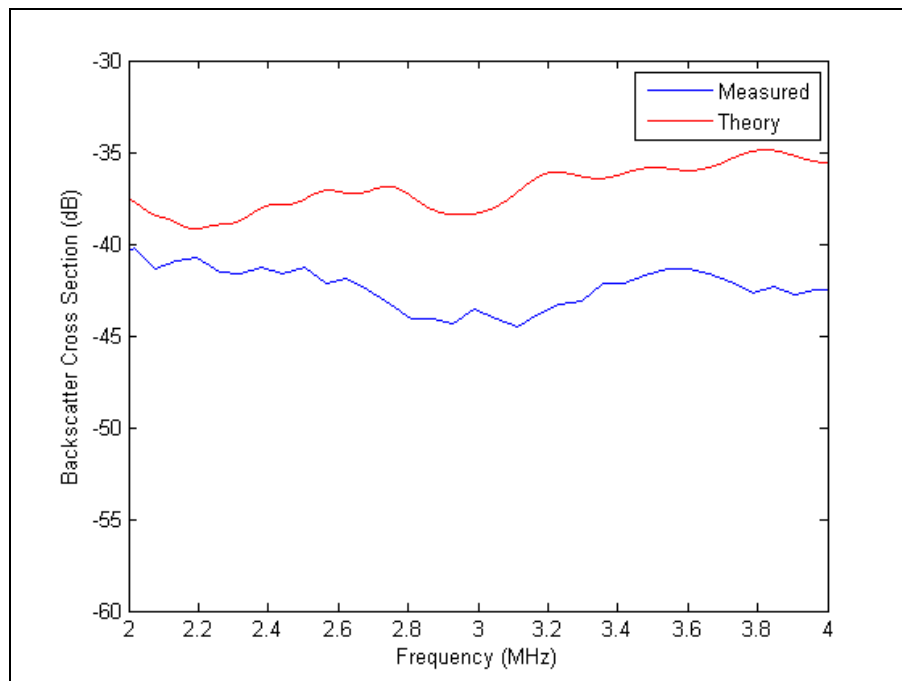
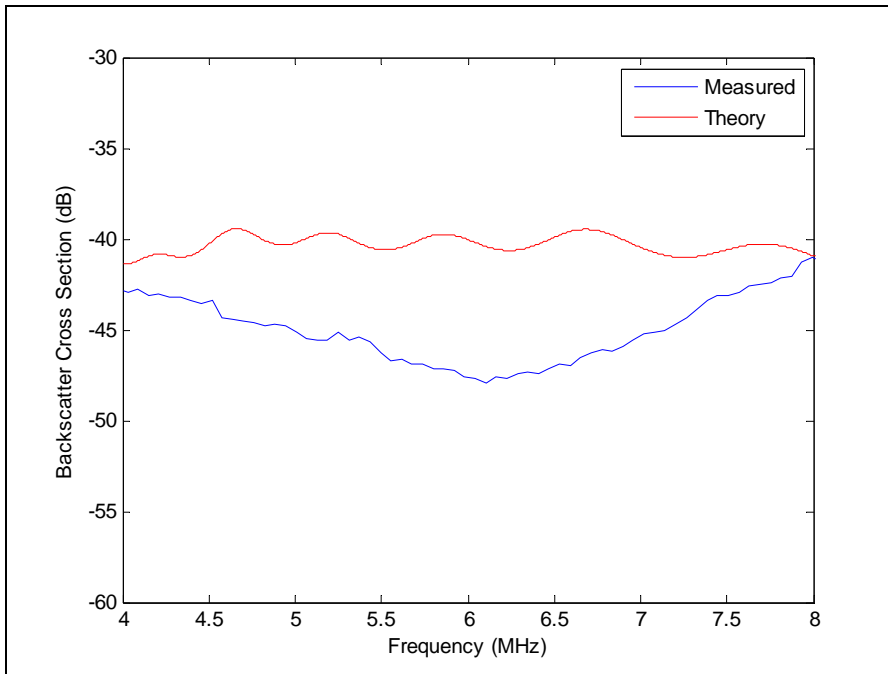
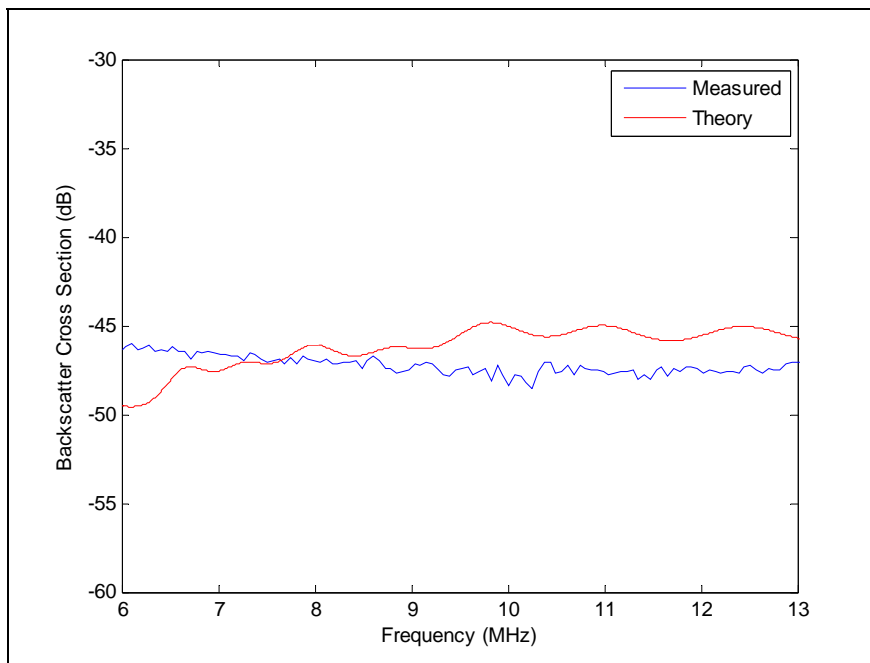


Figure 4.17 Theoretical vs. measured UCA backscatter cross section using 3 MHz transducer.



**Figure 4.18 Theoretical vs. measured UCA backscatter cross section using 6 MHz transducer.**



**Figure 4.19 Theoretical vs. measured UCA backscatter cross section using 10 MHz transducer.**

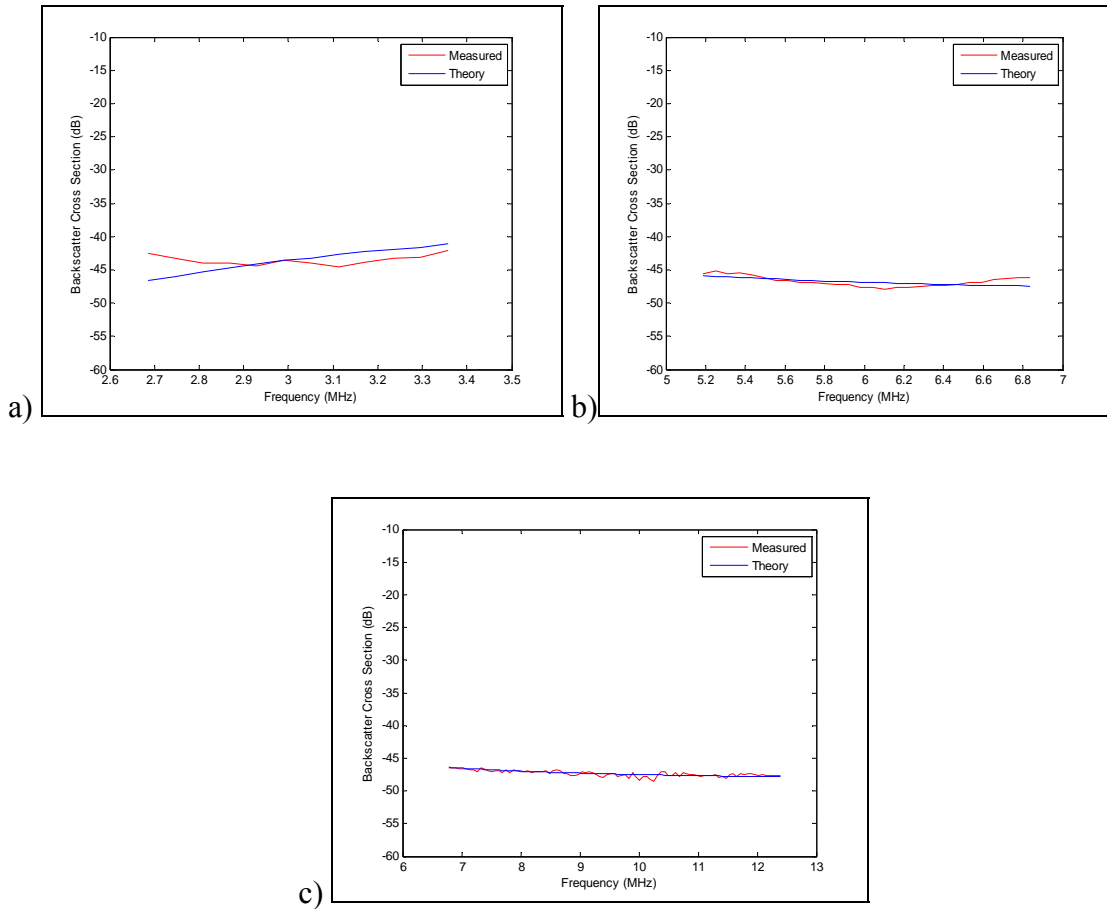


**Figure 4.20 Results of Monte Carlo fitting of the theoretical power spectra to (a) 3 MHz measured data set only, (b) 6 MHz measured data set only, and (c) 10 MHz measured data set only.**

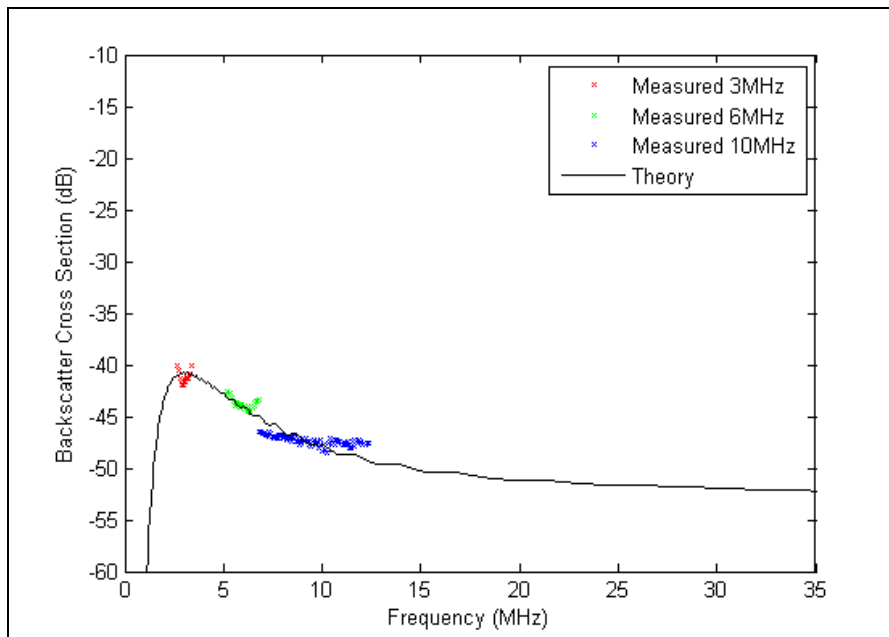


**Figure 4.21 Monte Carlo fitting of the theoretical power spectra to 3 MHz, 6 MHz, and 10 MHz measured data set simultaneously.**

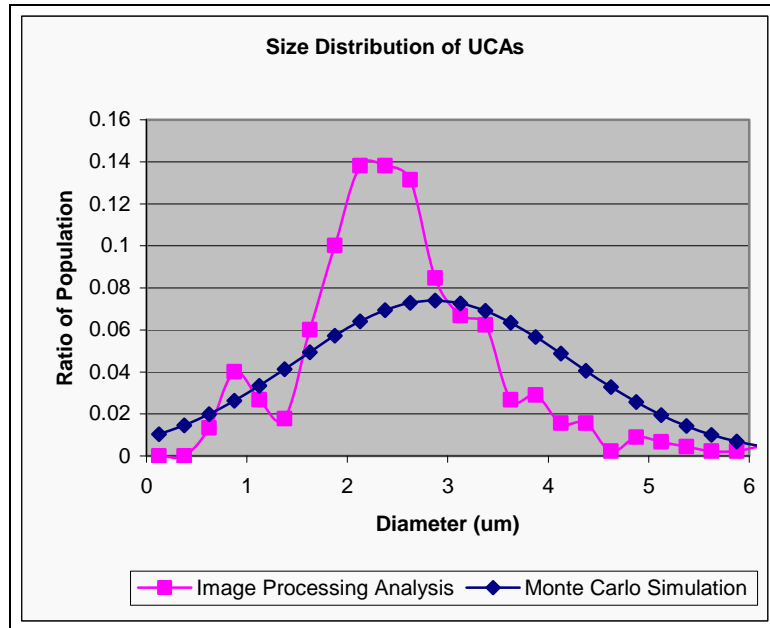


Figure 4.22 Comparing bubble size distributions obtained from Monte Carlo simulation and image processing analysis.

## 4.7 Tables

**Table 4.1 Half-life of Definity microbbles in degassed water at different concentrations and frequencies (measured in minutes).**

<i>3 MHz transducer</i>		
Concentration of Definity	After Vialmix	Out of Refrigerator
0.1x	6.604 ± 1.718	
1x	7.929 ± 0.998	
2x	8.046 ± 1.341	
<i>6 MHz transducer</i>		
Concentration of Definity	After Vialmix	Out of Refrigerator
0.1x	5.4 ± 1.253	5.695 ± 1.869
1x	6.118 ± 1.441	6.359 ± 1.929
2x	7.102 ± 1.071	6.756 ± 1.347
<i>10 MHz transducer</i>		
Concentration of Definity	After Vialmix	Out of Refrigerator
0.1x	7.484 ± 1.533	
1x	8.001 ± 1.4	
2x	6.99 ± 1.539	
<i>20 MHz transducer</i>		
Concentration of Definity®	After Vialmix	Out of Refrigerator
0.1x	5.802 ± 3.18	
1x	5.259 ± 2.082	
2x	6.163 ± 1.962	

**Table 4.2 T-test values comparing statistical significance of UCA half-life values at different transducer center frequencies.**

<i>Comparison</i>		T-test value,  t
<b>0.1x</b>	3 MHz vs. 6 MHz	0.981
	6 MHz vs. 10 MHz	1.823
	10 MHz vs. 20 MHz	0.825
<b>1x</b>	3 MHz vs. 6 MHz	1.790
	6 MHz vs. 10 MHz	1.623
	10 MHz vs. 20 MHz	1.893
<b>2x</b>	3 MHz vs. 6 MHz	0.953
	6 MHz vs. 10 MHz	0.103
	<b>10 MHz vs. 20 MHz</b>	0.574

**Table 4.3 T-test values comparing statistical significance of UCA half-life values at different concentrations of Definity microbubbles.**

<i>Comparison</i>		T-test value,  t
<b>3 MHz</b>	0.1x vs. 1x	1.155
	1x vs. 2x	0.121
	0.1x vs. 2x	1.146
<b>6 MHz</b>	0.1x vs. 1x	0.651
	1x vs. 2x	0.949
	0.1x vs. 2x	1.789
<b>10 MHz</b>	0.1x vs. 1x	0.431
	1x vs. 2x	0.842
	0.1x vs. 2x	0.394
<b>20 MHz</b>	0.1x vs. 1x	0.126
	1x vs. 2x	0.386
	<b>0.1x vs. 2x</b>	0.167

**Table 4.4 T-test values comparing statistical significance of UCA half-life values samples observed after Vialmix and out of refrigerator.**

<i>Comparison</i>		T-test value,  t
<b>0.1x</b>	After Vialmix vs. Out of Refrigerator	0.227
<b>1x</b>	After Vialmix vs. Out of Refrigerator	0.173
<b>2x</b>	After Vialmix vs. Out of Refrigerator	0.348

**Table 4.5 Half-life of 1x and 2x concentrations of Definity microbubbles when immersed in 0.9% saline solution and degassed water.**

<i>Concentration of Definity</i>	<i>After Vialmix</i>	<i>Out of Refrigerator</i>
<b>0.9% Saline Solution</b>		
1x	7.2278 ± 1.683	4.545 ± 0.6476
2x	9.3165 ± 2.896	5.8991 ± 0.6931
<b>Degassed Water</b>		
1x	6.118 ± 0.4412	6.359 ± 1.929
2x	7.702 ± 1.071	6.756 ± 1.347

**Table 4.6 T-test values comparing statistical significance of UCA half-life values in 0.9% saline solution vs. degassed water.**

<i>Comparison</i>	<i>T-test value,  t </i>
<b>After Vialmix</b>	
0.9% Saline Solution vs. Degassed Water (1x)	1.105
0.9% Saline Solution vs. Degassed Water (2x)	0.906
<b>Out of Refrigerator</b>	
0.9% Saline Solution vs. Degassed Water (1x)	1.544
<b>0.9% Saline Solution vs. Degassed Water (2x)</b>	0.980

**Table 4.7 Half-life for 0.1x concentration of Definity when transducer is switched off between snapshots and when transducer remained on (measured in minutes).**

<i>Concentration of Definity</i>	<i>After Vialmix</i>	<i>Out of Refrigerator</i>
<b>Transducer switch off between snapshots</b>		
0.1x	5.839 ± 0.2049	5.532 ± 0.9109
<b>Transducer remained on</b>		
0.1x	5.1 ± 1.253	5.695 ± 1.869

**Table 4.8 T-test values comparing statistical significance of UCA half-life values when transducer is switched off between snapshots and when transducer remained on.**

<i>Comparison</i>	<i>T-test value,  t </i>
<b>After Vialmix</b>	
Transducer switched off vs. remained on	1.001
<b>Out of Refrigerator</b>	
Transducer switched off vs. remained on	0.135

**Table 4.9 Backscattered power measurements within perfusion phantom.**

<b>Concentration</b>	<b>6 MHz Transducer</b>		<b>3 MHz Transducer</b>	
	<b>Backscatter Power (arbitrary units)</b>			
	<b>Average</b>	<b>Standard Dev</b>	<b>Average</b>	<b>Standard Dev</b>
0.1x	6.169E-5	4.406E-6	2.489E-5	8.957E-6
1x	2.354E-4	8.893E-6	7.699E-5	3.174E-5
2x	3.418E-4	5.490E-5	1.274E-4	4.559E-5

**Table 4.10 Ratio of initial UCA backscattered power measured within a beaker of degassed water.**

Ratio of Initial Backscattered Power	Concentration Ratios					
	Out of Refrigerator			After Vialmix		
	1x : 0.1x	2x : 1x	2x : 0.1x	1x : 0.1x	2x : 1x	2x : 0.1x
Transducer Frequency						
3 MHz				3.516	1.369	4.814
6 MHz	3.065	1.566	4.801	2.964	1.518	4.498
10 MHz				2.96	1.475	4.367
20 MHz				3.728	1.621	6.044

**Table 4.11 Ratio of initial UCA backscattered power measured within the perfusion phantom.**

Ratio of Initial Backscattered Power	Concentration Ratios		
	After Vialmix		
	1x : 0.1x	2x : 1x	2x : 0.1x
Transducer Frequency			
6 MHz	3.816	1.452	5.540
3 MHz	3.093	1.654	5.117

**Table 4.12 Microbubble count using a hemacytometer (numbers are given in 10<sup>4</sup>/mL).**

Concentration Ratios	0.1x	1x	2x
Trial #1	54.89	182.14	250.00
Trial #2	55.73	171.88	233.93
Trial #3	56.25	156.94	295.00
Trial #4	62.00	183.93	325.00
<b>Average</b>	<b>57.22</b>	<b>173.72</b>	<b>275.98</b>
<b>Expected concentration</b>	<b>9.6</b>	<b>96</b>	<b>192</b>
<b>Standard Deviation</b>	<b>3.237</b>	<b>12.38</b>	<b>41.66</b>

**Table 4.13 Comparison of ratio of microbubble concentrations measured from hemacytometer and UCA backscattered power.**

Ratio of Initial Backscattered Power Transducer Frequency	Concentration Ratios		
	1x : 0.1x	2x : 1x	2x : 0.1x
<b>Within a Beaker</b>			
6 MHz	2.964	1.518	4.498
3 MHz	3.516	1.369	4.814
10 MHz	2.96	1.475	4.367
20 MHz	3.728	1.621	6.044
<b>Within a Perfusion Phantom</b>			
6 MHz	3.816	1.452	5.540
3 MHz	3.093	1.654	5.117
<b>Hemacytometer Count</b>			
Measured Ratios	3.036	1.589	4.823

**Table 4.14 Mean diameter and standard deviation of UCAs “After Vialmix” and “30 min after Vialmix.”**

<i>Diameter</i>	<i>After Vialmix</i>	<i>30 minutes after Vialmix</i>
<b>Spatial Domain Analysis (<math>\mu\text{m}</math>)</b>	2.636 $\pm$ 0.44	1.439 $\pm$ 0.107
<b>Fourier Domain Analysis (<math>\mu\text{m}</math>)</b>	2.489 $\pm$ 0.41	1.373 $\pm$ 0.075

**Table 4.15 Average diameter of microbubbles over 35 min.**

<i>Time (min)</i>	<i>Average Diameter (<math>\mu\text{m}</math>) (spatial domain analysis)</i>	<i>Average Diameter (<math>\mu\text{m}</math>) (Fourier domain analysis)</i>
0	4.311 $\pm$ 1.379	4.143 $\pm$ 1.454
5	3.322 $\pm$ 2.403	3.159 $\pm$ 0.753
10	2.691 $\pm$ 1.656	2.537 $\pm$ 0.576
15	2.484 $\pm$ 1.261	2.336 $\pm$ 1.671
30	1.831 $\pm$ 1.529	1.768 $\pm$ 0.673
<b>35</b>	1.688 $\pm$ 1.339	1.496 $\pm$ 0.298

**Table 4.16 In vivo backscattered power ratios.**

<b>Concentration Ratios</b>	<b>2x:1x</b>	<b>5x:2x</b>	<b>5x:1x</b>
<b>Measured Backscatter Power Ratio</b>	1.741	2.992	5.211
<b>Expected Ratio</b>	2	2.5	5
<b>Percentage Error (%)</b>	12.95	19.68	4.22

**Table 4.17 Comparing mean, variance and UCA concentration estimates obtained using hemacytometer/image processing analyses and Monte Carlo simulation.**

	<b>Mean UCA Radius (<math>\mu\text{m}</math>)</b>	<b>UCA Variance (<math>\mu\text{m}</math>)</b>	<b>Concentration (<math>10^6/\text{mL}</math>)</b>
<b>Hemacytometer/Image Processing Analyses</b>	1.32	0.193	1.737
<b>Monte Carlo Simulation</b>	1.432	0.477	1.951
<b>Percentage Error (%)</b>	8.48	147	12.3

## **CHAPTER 5: CONCLUSIONS AND FUTURE WORK**

### **5.1 In Vitro Experiments**

#### **5.1.1 Beaker experiments**

Through the in vitro beaker experiments, we were able to quantify and monitor the exponential decay in backscatter from Definity microbubbles backscatter in degassed water, 0.9% saline solution, and blood. Experiments indicated that this decay was an intrinsic property of the microbubbles independent of medium, pressure induced by the acoustic field, frequency, or UCA concentration. The half-life of Definity microbubbles varied between 5 and 8 min. With such volatility in the backscattered power over time, obtaining good results became contingent on being able to prepare and observe samples within a consistent time frame and to adjust the size, variance, and concentration of UCAs using a model fitting routine. This may alone have implications for establishing dose-effect curves because the concentration of UCAs in the bloodstream are constantly changing and therefore need to be monitored in real time.

Analysis of the initial backscattered power also indicated that we were able to differentiate between microbubble concentrations (i.e., larger concentrations of Definity resulted in larger backscattered power and vice versa) as well as time lapse since Vialmix activation. The larger initial backscattered power from samples used immediately after Vialmix activation compared to those taken out of the refrigerator suggested a population of UCAs consisting of larger microbubbles in the samples used immediately after Vialmix activation. This was later confirmed optically.

Experiments conducted in blood revealed an inverse relationship between backscattered power and blood hematocrit value (i.e., an increase in hematocrit value resulted in a decrease in backscattered power). Literature as well as simulation results confirmed this relationship. However, results obtained in this study were of a qualitative nature only, simply showing the existence of the relationship between backscattered power and hematocrit value. Further work is needed to obtain more accurate estimates of density, viscosity, and speed of sound in blood as a function of hematocrit value. In addition, to accurately predict the backscatter cross section of UCAs in blood, attenuation in blood must be compensated. Adequate estimates for these values will lead to a more

comprehensive understanding of the mechanism responsible for the relationship between blood hematocrit value and UCA backscatter.

### **5.1.2 Perfusion phantom experiments**

Even through 1/16 inch of silicone tubing, the results of the backscatter measurements suggested that the presence of microbubbles could be detected within the perfusion phantom and the relative concentrations of Definity microbubbles could be estimated. Larger concentrations of Definity backscattered more power and vice versa. In theory, the ability to quantify microbubbles in motion in vitro should correlate to quantifying microbubbles in vivo effectively. The contribution of Doppler shifts to the frequency of the backscattered power spectra was found to be insignificant and therefore would not affect estimates of the UCA concentration.

## **5.2 In Vivo Experiments**

In vivo experiments verified the capability to detect microbubbles within the central auricular artery of a New Zealand white rabbit using a 20 MHz transducer. Results also indicated the ability to differentiate between relative concentrations of Definity. The relatively small cross section of the auricular artery often restricted the ability to quantify UCAs properly. As such, many of the data sets collected were contradictory and discarded. Good data sets were acquired, which confirmed the linear relationship between backscattered power and UCA concentration. The ability to image a larger artery, such as the aorta, would reduce the number of discarded data sets because the size of the vessel could be easily resolved. The results suggest that resolving the blood vessel is important to establishing a good estimation technique. Nevertheless, the in vivo results clearly support the possibility of quantifying UCAs noninvasively. The next phase is to isolate the backscattered power due to the UCAs given the backscatter data of the microbubbles in blood and backscatter data from blood without microbubbles, and to examine the use of the technique in other vessels.

### **5.3 Concentration of UCA Population**

Through hemacytometer analysis, concentration values were assigned to the so-called 0.1x, 1x, and 2x concentrations. These concentration measurements exposed errors in the sample preparation technique, but in doing so confirmed the linear relationship between concentration of microbubbles and backscattered power in the beaker and perfusion phantom experiments. That is, a three-fold increase in concentration should result in a three-fold increase in UCA backscattered power. The ratio of concentrations remained relatively consistent between different transducers, which suggested that quantification of microbubbles was independent of frequency. In addition, perfusion phantom experiments suggested that even when in motion, microbubble concentrations could be quantified. Agreement with theory gave rise to the possibility of quantifying relative concentrations of UCAs in vitro.

### **5.4 Theory vs. Measured Backscatter Cross Section**

Plotting the theoretical backscatter cross section against the measured data using the 3 MHz and 6 MHz transducer revealed a maximum -7 dB difference between theory and measurement. Assuming the size distribution of microbubbles is accurate, this result suggested that UCA concentration could be estimated to within a factor of five. These are not perfect results but they are encouraging, illustrating that it is possible to quantify UCAs in vitro.

Monte Carlo simulation results indicated that the mean microbubble radius and concentration in vitro could be estimated to within 8.48% and 12.3%, respectively. Now that it can be shown that this Monte Carlo simulation technique works in vitro, the next phase is to show its effectiveness in vivo. More efficient methods of curve fitting may be useful in the rapid and accurate estimation of the UCA concentration and could be the subject of future work.

As expected, the effectiveness of this technique heavily depends on the accuracy of the measured data. As the experiments indicated, the backscattered power from the Definity microbubbles is highly time-dependent, decaying quickly over time. In some cases, within even a 5 min window the backscattered power dropped by 50%. The consequence in this drop is a possible ~6 dB error or a factor of two error in UCA

concentration estimates simply because preparing the UCA sample took a little longer than usual. Such factors must be taken carefully into consideration when using the Monte Carlo simulation for providing in vivo estimates.

## **5.5 Future Work**

In this study, relatively good correlation between theory and measured data for in vitro experiments was observed. However, the eventual goal is to be able to quantify UCAs in situ. For this goal to be realized, future work needs to be invested in understanding the backscatter properties of UCAs in blood. Because of the poor quality of the in vivo data acquired, serious consideration should be invested in revamping the data acquisition procedure. Instead of imaging the contrast agents within the central auricular artery, which, because of its size, limits the number of UCAs within the gated volume of the active transducer, larger arteries/veins should be considered. Work is currently in progress to switch from a single-element transducer to a transducer array for the in vivo experiments. This should allow for deeper penetration into the body and imaging of larger arteries such as the aorta. Given the relative success of the Monte Carlo simulations at predicting mean bubble radius and concentration, this technique can still be used to quantify UCAs in vivo. This, of course, is contingent on a good theoretical model of UCA backscatter in vivo. More complex curve fitting routines may be necessary to evaluate the UCA concentration in real time.

## REFERENCES

- [1] V. Sboros, "Response of contrast agents to ultrasound," *Advanced Drug Delivery Reviews*, vol. 60, pp. 1117-1136, 2008.
- [2] N. de Jong and L. Hoff, "Ultrasound scattering properties of Albnunx microspheres," *Ultrasonics*, vol. 31, pp. 175-181, 1993.
- [3] P. J. A. Frinkling and N. de Jong, "Acoustic modeling of shell-encapsulated gas bubbles," *Ultrasound in Medicine & Biology*, vol. 24, pp. 523-533, 1998.
- [4] P. J. A. Frinkling, N. de Jong, and E. I. Cespedes, "Scattering properties of encapsulated gas bubbles at high ultrasound pressures," *Journal of the Acoustic Society of America*, vol. 105, pp. 1989- 1996, 1999.
- [5] S. Hernot and A. L. Klibanov, "Microbubbles in ultrasound-triggered drug and gene delivery," *Advanced Drug Delivery Reviews*, vol. 60, pp. 1153-1166, 2008.
- [6] P. A. Dayton, K. E Morgan, A. L. Klibanov, G. H. Brandenburg, and K. W. Ferrara, "Optical and acoustical observations of the effects of ultrasound on contrast agents," *IEEE Transactions on Ultrasonics, Ferroelectrics, and Frequency Control*, vol. 46, pp. 220-232, 1999.
- [7] D. E. Geortz, N. de Jong, and A. W. F. van der Steen, "Attenuation and size distribution measurements of Definity and manipulated Definity populations," *Ultrasound in Medicine & Biology*, vol. 33, pp. 1376-1388, 2007.
- [8] S. L. Bridal, O. Lucidarme, J-M. Correas, P. N. Burns, J-F. Moreau, and G. Berger, "Quantification of ultrasound contrast agent in an in vitro perfusion phantom," *IEEE Ultrasonics Symposium*, vol. 2, pp. 1759-1762, 1999.
- [9] M. F. Insana, T. J. Hall, R. F. Wagner, and D. G. Brown, "Describing small-scaled structure in random media using pulse-echo ultrasound," *Journal of the Acoustical Society of America*, vol. 87, pp. 179-192, 1990.
- [10] L. E. Kinsler and A. R. Frey, *Fundamentals of Acoustics*. New York, NY: John Wiley & Sons, Inc., 1950.
- [11] M. F. Insana and T. J. Hall, "Parametric ultrasound imaging from backscatter coefficient measurements: Image formation and interpretation," *Ultrasonic Imaging*, vol. 12, pp. 245-267, 1990.
- [12] H. Medwin, "Counting bubbles acoustically: A review," *Ultrasonics*, vol. 15, pp. 7-13, 1977.

- [13] N. de Jong, L. Hoff, T. Skotland, and N. Bom, "Absorption and scatter of encapsulated gas filled microspheres: Theoretical considerations and some measurements," *Ultrasonics*, vol. 30, pp. 95-103, 1992.
- [14] A. A. Doinikov, J. F. Haac, and P. A. Dayton, "Resonance frequencies of lipid-shelled microbubbles in the regime of nonlinear oscillations," *Ultrasonics*, vol. 49, pp. 263-268, 2009.
- [15] T. G. Leighton, *The Acoustic Bubble*. San Diego, CA: Academic Press, 1994.
- [16] R. Cornet, N. de Jong, and C. T. Lancee, "Higher harmonics of vibrating gas-filled microspheres. Part one: Simulations," *Ultrasonics*, vol. 32, pp. 447-453, 1994.
- [17] C. Devin, "Surveying of thermal, radiation, and viscous damping of pulsating air bubbles in water," *Journal of the Acoustical Society of America*, vol. 31, pp. 1654-1667, 1959.
- [18] M. O'Donnell and J. G. Miller, "Quantitative broadband ultrasonic backscatter: An approach to nondestructive evaluation in acoustically inhomogeneous materials," *Journal of Applied Physics*, vol. 52, pp. 1056-1065, 1981.
- [19] D. Chatterjee, K. Sarkar, P. Jain, and N. E. Schreppler, "On the suitability of broadband attenuation measurement for characterizing contrast microbubbles," *Ultrasound in Medicine & Biology*, vol. 31, pp. 781-786, 2005.
- [20] A. Haak, R. Lavarello, and W. D. O'Brien, Jr., "Semiautomatic detection of microbubble ultrasound contrast agent destruction applied to Definity using support vector machines," in *Proceedings - IEEE Ultrasonics Symposium, 2007*, pp. 660-663.
- [21] W. T. Shi, F. Forsberg, A. Tornes, J. Ostensen, and B. B. Goldberg, "Destruction of contrast microbubbles and the association with inertial cavitation," *Ultrasound in Medicine & Biology*, vol. 26, pp. 1009-1019, 2000.
- [22] V. Sboros, C. A. MacDonald, S. D. Pye, C. M. Moran, J. Gomatam, and W. N. McDicken, "The dependence of ultrasound contrast agents backscatter on acoustic pressure: Theory versus experiment," *Ultrasonics*, vol. 40, pp. 579-583, 2002.
- [23] J. F. Zachary, J. P. Blue, R. J. Miller, and W. D. O'Brien, Jr., "Vascular lesions and S-thrombomodulin concentrations from auricular arteries of rabbits infused with microbubble contrast agent and exposed to pulsed ultrasound," *Ultrasound in Medicine & Biology*, vol. 32, no. 11, pp. 1781-1791, 2006.

- [24] D. W. Droste, "Clinical utility of contrast-enhanced ultrasound in neurosonology," *European Neurology*, vol. 59, pp. 2-8, 2008.
- [25] K. K. Shung, "Physics of blood echogenicity," *Journal of Cardiovascular Ultrasonography*, vol. 2, pp. 401-406, 1983.
- [26] S. H. Wang, Y. H. Lin, and K. K. Shung, "In vivo measurements of ultrasonic backscatter from blood," *IEEE Ultrasonics Symposium*, vol. 2, pp. 1161-1164, 1997.